Muted orbital-scale Monsoon Variability over the Korean Peninsula

Nitesh Sinha[1,2], Axel Timmermann[1,2], Sun-Seon Lee[1,2], Kyoung-Nam Jo[3], Jasper A. Wassenburg[1,2], Daniel M. Cleary[1,2], Kyung-Sook Yun[1,2]

[1]Center for Climate Physics, Institute for Basic Science, Busan, Republic of Korea
[2]Pusan National University, Busan, Republic of Korea
[3]Kangwon National University, Chuncheon, Gangwon-do, Republic of Korea

Correspondence to: Nitesh Sinha (nitesh@pusan.ac.kr)

Abstract. A recent study identified an east-west dipole pattern in Asian Summer Monsoon precipitation and in its oxygen-isotope composition variability in response to orbital forcing (Wen et al., 2024). The Korean Peninsula (KP) is situated near the nodal line of this dipole and should therefore exhibit muted precessional variability in both. So far, this conjecture has not been tested using paleoclimatic data. Here, we present speleothem oxygen isotope ($\delta^{18}O$) records from the KP, which support the notion of suppressed orbital-scale hydroclimate variability. Conducting a transient model simulation with the isotope-enabled Community Earth System Model (iCESM1.2) covering the past 130,000 years, along with tagging experiments for low and high insolation conditions, we show that, on precessional timescales, isotopic contributions from oceanic and continental moisture sources compensate each other over the KP, resulting in only a weak regional signal in precipitation $\delta^{18}O$. Based on iCESM1.2 simulations, we further demonstrate that deuterium excess (d-excess) variability over the KP would still capture the moisture source region's zonal seesaw response to precessional forcing. We propose that, given the region's strong sensitivity to changes in moisture sources, paleo-water d-excess reconstructions from East Asia speleothems could provide valuable additional constraints on the drivers of regional monsoon systems. This study offers new insights into the spatiotemporal variability of Pan-Asian hydroclimates and its links to changes in moisture source.

Deleted: East
Deleted: (EASM)
Deleted: precessional-scale
Deleted: . It
Deleted: precipitation and its oxygen isotope composition ($\delta^{18}O_p$)
Deleted: $\delta^{18}O$ ($\delta^{18}O_{sp}$)
Deleted:
Deleted: $\delta^{18}O_p$
Deleted: ,
Moved (insertion) [1]
Deleted: indicating that the reconstruction of paleo water d-excess values from eastern Asian speleothem fluid inclusions could provide new valuable insights into the drivers of regional monsoon systems.
Deleted: provides
Moved up [1]: This study provides new insights into the spatiotemporal variability of Pan-Asian hydroclimates and its links to changes in moisture source.

1 Introduction

Speleothem (secondary carbonate deposits in caves) records, leveraged by radiometrically constrained chronologies, have been a valuable resource for reconstructing paleo-hydroclimate variability in tropical and subtropical regions (Braun et al., 2019; Cai et al., 2015; Cheng et al., 2016; Gasse et al., 2011; Jo et al., 2017; Maher and Thompson, 2012). Such work is predicated on stable oxygen isotope ($\delta^{18}O$) measurements of speleothem calcite ($\delta^{18}O_c$), which ultimately derives from atmospheric moisture. When speleothem $CaCO_3$ precipitates under near-equilibrium conditions, $\delta^{18}O_c$ encodes cave air temperature and drip water $\delta^{18}O$. Drip water typically reflects the $\delta^{18}O$ of precipitation ($\delta^{18}O_p$), integrating processes such as Rayleigh fractionation along water-vapor pathways and, in some regions, the amount of regional rainfall (Lachniet, 2009). In regions where large changes in $\delta^{18}O_p$ are expected with respect to the effect of temperature, $\delta^{18}O_c$ is often considered as an indicator of atmospheric variability. Considering $\delta^{18}O_c$ as an indicator of atmospheric variability, $\delta^{18}O_c$-records from Chinese caves (e.g., Cheng et al., 2009; Wang et al., 2001) have provided key insights into seasonal and centennial-to-orbital-scale variability in the Asian monsoon system. Speleothems that grew within the two sub-monsoon branches of this system, the Indian Summer Monsoon (ISM) and the East Asian Summer Monsoon (EASM), generally show a close correspondence in their $\delta^{18}O_c$ variability (Cai et al., 2015; Cheng et al., 2019; Kathayat et al., 2016), at least on orbital timescales. The relationship was initially interpreted as an illustration of large-scale in-phase variations in atmospheric processes across both monsoons (Cheng et al., 2009, 2016; Kathayat et al., 2016; Wang et al., 2001). However, unlike the ISM, the EASM is characterized by more complex spatial patterns in precipitation and in $\delta^{18}O_p$, even under present-day climate conditions (Chiang et al., 2017; Wang et al., 2008; Zhao et al., 2012).

Our current understanding is that the EASM precipitation pattern is mainly driven by the

Deleted: -
Deleted: s
Deleted: p
Deleted: under
Deleted: s
Deleted: p
Deleted: s
Deleted: p
Deleted: $\delta^{18}O_{sp}$
Deleted: $\delta^{18}O_{sp}$
Deleted: $\delta^{18}O_{sp}$
Deleted: systems

position of the subtropical front, which responds to Northern Hemispheric Summer Insolation (NHSI). The frontal system, established through interactions between the Westerly jet and the Western North Pacific Subtropical High (WNPSH), separates moist tropical air masses and drier, colder extratropical air masses. The front is a primary rain-producing feature (Meiyu-Baiu rainband, or Changma for the Korean Summer Monsoon) in the EASM (Chen and Chang, 1980; Ding, 2004; Wang et al., 2008), and it controls the seasonality (Hu et al., 2019; Liu et al., 2022; Wang et al., 2008), rainfall distribution, intensity, and extent of the moisture advection from tropical oceans (Lin et al., 2024; Volonté et al., 2022).

Speleothem-based studies, complemented by climate simulations, have reported a connection between the EASM's characteristics (intensity and pattern) and frontal movements across different timescales and under extreme climatic conditions (Chiang et al., 2015; Liu et al., 2014; Volonté et al., 2022; Wang et al., 2008; Wu et al., 2018). For instance, Liu et al., (2014) demonstrate that frontal interactions with synoptic weather lead to heavier rainfall in northern China during high NHSI (boreal summer perihelion conditions). Later studies have reported wetter conditions in central-eastern China and spatially opposite rainfall signals across Asia during the last deglaciation (Termination I), in association with shifts in the position of the Westerlies (He et al., 2021; Zhang et al., 2018). A recent study by Xue et al. (2025) proposed that WNPSH intensity played a key role in shaping hydrological conditions across central China over various timescales.

On precessional timescales, a significant correlation exists between variability in Asian speleothem $\delta^{18}O_c$ records and NHSI, indicating that the latter primarily controls the large-scale circulation of the Asian summer monsoon and its associated moisture transport. Chinese speleothem $\delta^{18}O_c$ has commonly been interpreted as reflecting changes in large-scale monsoon circulation, integrated moisture transport, and upstream rainout processes, rather than local

Deleted: Liu et al.

Deleted: (

Deleted: ,

Deleted: or

Deleted: the

Deleted: of the WNPSH

Deleted: at

Deleted: On precessional timescales, a significant correlation between variability in Chinese $\delta^{18}O_{sp}$ and NHSI implies a dominant control of the latter on the EASM

Formatted: Subscript

Formatted: Subscript

precipitation amount alone (Cai et al., 2015; Cheng et al., 2016; Kathayat et al., 2016; Wang et al., 2001). The interpretation of Chinese speleothem $\delta^{18}O_c$ as a proxy for local precipitation amount remains debated because independent precipitation-sensitive proxies from East Asia, such as loess magnetic susceptibility and reconstructed seawater $\delta^{18}O$ (Beck et al., 2018; Clemens et al., 2018; Sun et al., 2006; Zheng et al., 2022), show only a weak correspondence with the precessional cycle. Cheng et al. (2021) addressed the discrepancies and complexities of hydroclimate proxies in Eastern Asia, explaining that loess, marine, and cave records are complementary and preferentially capture specific aspects of Asian monsoon dynamics. Further supported by Li et al. (2024), who found that the ratio of dithionite−citrate−bicarbonate extractable iron to total iron in Chinese loess deposits potentially records precipitation cycles on precessional timescales. However, uncertainties in interpreting the magnetic-susceptibility-based reconstructions remain, as they might reflect a smoothed precipitation signal or be dominated by other forcings (Cheng et al., 2021; Sun and Huang, 2006).

Climate model simulations generally show enhanced Asian summer monsoon precipitation under stronger NHSI (Bosmans et al., 2018), although the magnitude of the simulated response may differ from that inferred from paleoclimate evidence (Lee et al., 2019). Isotope-enabled modeling offers an opportunity to further evaluate the roles of atmospheric, land, and oceanic processes in a changing climate (i.e., transient simulations). They can help interpret precipitation-based proxies by tracing the stable isotopologues of water spatiotemporally (Battisti et al., 2014; Brady et al., 2019; Cheng et al., 2021). Such modeling studies have also shown that other processes may dominate on $\delta^{18}O_p$ more than the Amount effect, including atmospheric circulation, moisture pathways, and upstream rainout (Liu et al., 2014; Maher and Thompson, 2012; Pausata et al., 2011). Subsequent studies have examined the complex relationships among orbital-scale EASM $\delta^{18}O$ variability, NHSI, rainy seasons, and regional circulation patterns (Dai et al., 2021; Liu et al., 2022; Yang et al., 2024). Though the major

Deleted: , as the former has been interpreted as an indicator of recorded changes in the EASM

Deleted: This interpretation

Deleted: has, however, been challenged by other regional precipitation-based proxies

Deleted: (e.g., loess magnetic susceptibility, seawater $\delta^{18}O$)

Deleted: which

Deleted: (Bosmans et al., 2018)(Lee et al., 2019)(Liu et al., 2014; Maher and Thompson, 2012; Pausata et al., 2011)

Deleted: Previous

Deleted: isotope modeling studies have discussed the complex relationship between orbital-scale EASM $\delta^{18}O_p$

features of simulated climate-isotopic signals across southern and eastern Asia agree with Chinese speleothem isotope records, some models suggest a pronounced out-of-phase precipitation response between the EASM rainband and the rest of the Asian monsoon on orbital timescales (Bosmans et al., 2018; Hu et al., 2019). Some isotope-enabled climate models also reveal large-scale differences in the response of $\delta^{18}O_p$ to precessional forcing across Asia, with weaker anomalies over the eastern domain than over the western domain (Battisti et al., 2014; Tabor et al., 2018). A recent study elucidated the mechanisms by which the precession-driven insolation forcing reorganizes the large-scale Asian summer monsoon circulation, including the strength of the southwesterly monsoon flow, the position of the upper-level westerly jet, and the position and strength of WNPSH, thereby altering regional precipitation and the relative contributions of remote and nearby moisture sources to $\delta^{18}O_p$ (Wen et al., 2024). These processes produce a grand dipole pattern of precipitation and $\delta^{18}O_p$ variability across the Asian monsoon region, characterized by an antiphase precipitation pattern between South Asia and Japan. This pattern suggests that precipitation variability on precessional timescales may be weaker over nodal regions such as the Korean Peninsula (KP).

The KP lies at the boundary between northeast Asia and the Pacific, and moisture transport through the WNPSH strongly controls summer precipitation variability over the region (Ha et al., 2012; Wang and Lin, 2002). Under present-day conditions, precipitation isotope compositions over these regions are influenced by seasonal shifts in atmospheric circulation that alter moisture source regions, moisture transport pathways, and the associated upstream rainout history during transport (Araguás-Araguás et al., 1998; Jung et al., 2022; Kim et al., 2019; Zhu et al., 2023). Studies have suggested that variations in $\delta^{18}O_p$ over KP are strongly influenced by seasonal changes in atmospheric circulation and moisture transport, as reflected in the pronounced seasonality of precipitation deuterium excess (d-excess) (Lee et al., 2001; Park et al., 2006). The seasonal cycle in d-excess primarily reflects changes in climatic

Deleted: I

Deleted: A recent study elucidated the mechanisms underlying precession-scale EASM precipitation and $\delta^{18}O_p$ variability and identified a grand dipole response pattern to orbital forcing (Wen et al., 2024), which predicts weaker precessional variability over the nodal regions, such as the Korean Peninsula (KP).

Deleted: In the context of observed variations in $\delta^{18}O_p$, precipitation isotope compositions in these areas may be influenced by various air masses and are primarily determined by moisture sources

Deleted: Studies have suggested that the moisture source predominantly drives $\delta^{18}O_p$ over the KP, as inferred from the strong seasonality in deuterium excess (d-excess) in present-day records

Deleted: , K.S.

Deleted: , Y.

conditions in the moisture-evaporation region, particularly relative humidity during evaporation. Further, d-excess can also be modified by changes in dominant air masses and moisture transport pathways, as well as secondary processes such as condensation and raindrop evaporation. Consequently, the seasonal contrast in precipitation d-excess, with generally lower values in summer and higher values in winter, has been associated with the distinct climatic conditions accompanying the EASM and East Asian winter monsoon, respectively (Yoshimura and Ichiyanagi, 2009).

While many studies (Clemens et al., 2018; Hayashi et al., 2017, 2021; Igarashi and Oba, 2006; Iwamoto and Inouchi, 2007; Wen et al., 2024) have extensively examined the eastern boundary of the EASM system, the KP has received less attention. We close this gap in our study by focusing on variations in $\delta^{18}O_p$ over the KP and their underlying mechanisms, aiming to enhance our understanding of the pan-Asian monsoon system. Here, we explore the dynamics by tracking and quantifying the moisture sources and their precessional modulation of seasonal rainfall and isotopes over the KP. To this end, we consider the Korean stalagmites' 550,000-year $\delta^{18}O_c$ records (discontinuous), which include a new $\delta^{18}O_c$ record from the Eden Cave stalagmite (ED1) and previously published $\delta^{18}O_c$ records from Gwaneum Cave stalagmite (GE1) (Jo et al., 2010, 2014). To link large-scale atmospheric circulation, moisture transport, and precipitation isotope variability over the KP on orbital timescales, we conducted a series of transient climate simulations, time-slice experiments, and water-tagging simulations using the isotope-enabled Community Earth System Model version 1.2 (iCESM1.2), focusing solely on the effect of orbital forcings. The transient simulation with an orbital acceleration (Lorenz and Lohmann, 2004a) of 100 spans the past 130,000 years (130 ka). The iCESM1.2 time-slice simulations were conducted with fixed minimum and maximum values of the precession index, reflecting Northern Hemisphere summer perihelion and aphelion conditions, respectively. The results are further interpreted using previously conducted high-resolution CESM1.2

Deleted: The seasonality of d-excess is primarily attributed to oceanic airmass in summer (low d-excess) and the interaction between a relatively warm oceanic airmass and a cold, dry continent air in winter (high d-excess)

Deleted: extensively

Deleted: of

Deleted: $\delta^{18}O$ ($\delta^{18}O_{sp}$ and

Deleted:)

Deleted: n

Deleted: To this end, we consider new and previously published $\delta^{18}O_{sp}$ records from two Korean stalagmites: ED1 (Eden Cave, (Jo et al., 2014)) and GE1 (Gwaneum Cave, (Jo et al., 2010))

Deleted: Moreover, to elucidate how large-scale changes in circulation and moisture sources influence $\delta^{18}O_p$ variations over the KP on orbital timescales, we conducted a series of transient climate and time-slice simulations and water-tagging experiments. These simulations utilized

Deleted:

Deleted: and focused

Deleted: n

Deleted: h

simulations (Chu et al., 2020; Huang et al., 2021; Raavi et al., 2023; Wengel et al., 2021) and a lower resolution transient CESM1.2 simulation, which includes orbital, greenhouse gas, and ice sheet forcings (Timmermann et al., 2022; Yun et al., 2023).

2 Materials and Methods

2.1 South Korean Speleothem Records

We present $\delta^{18}O_c$ records from two Korean stalagmites obtained from ED (Eden Cave (Jo et al., 2014)) and GE (Gwaneum Cave (Jo et al., 2010)) (see locations in Fig. 1 and Fig. 2a), which grew intermittently. The $\delta^{18}O_c$ records for ED1 and GE1 stalagmites were previously measured along with stable carbon isotope ($\delta^{13}C_c$) within the scope of Jo et al. (2010, 2014). However, the ED1 $\delta^{18}O_c$ record remained unpublished to date. Further details regarding the GE1 and ED1 records and their covered time spans are provided in Supplementary Table S1.

Previous studies of the ED1 and GE1 stalagmites documented their growth fabrics, depositional histories, stable cave environment, and stable-isotope characteristics, thereby constraining the conditions under which their isotopic signals were preserved. The principal growth phase of GE1 was interpreted to have formed under conditions approaching isotopic equilibrium, based on its calcite textures and stable-isotope characteristics, whereas intervals associated with coralloid growth and limited dripwater supply were identified as distinct depositional phases (Jo et al., 2010). ED1, similarly, contains well-characterized growth intervals separated by hiatuses and changes in depositional fabric, supported by an extensive U-series chronology (Jo et al., 2006, 2014). Although certain intervals exhibit high $\delta^{18}O_c$ variability, partially due to the low resolution of the records, the absence of a pronounced precessional cycle is notably observed in the $\delta^{18}O_c$ profiles (Fig. S1). From another Korean cave, Jo et al. (2017) identified clear millennial-scale resemblances among late Holocene $\delta^{18}O_c$ records from both Korean and Chinese stalagmites, providing an in-depth discussion on the issue in question. These

Deleted: s
Deleted: $\delta^{18}O_{sp}$
Deleted: $\delta^{18}O_{sp}$
Deleted: 1
Deleted: 1
Deleted: (Fig. S1)
Deleted: $\delta^{18}O_{sp}$
Deleted: $_{sp}$
Deleted: $\delta^{18}O_{sp}$
Deleted: remained
Deleted: this
Formatted: Font: (Asian) +Body Asian (Malgun Gothic)
Deleted: (Jo et al., 2010, 2014, 2006)
Formatted: Font: Not Bold
Formatted: Font: Not Bold, Subscript
Formatted: Font: Not Bold
Formatted: Font: Not Bold
Formatted: Font: Not Bold
Deleted: (Jo et al.,
Deleted:)
Formatted: Font: Not Bold, Subscript
Formatted: Font: Not Bold
Formatted: Font: Not Bold
Formatted: Font: Not Bold
Formatted: Font: Not Bold, Subscript
Formatted: Font: Not Bold

observations suggest that, despite potential site-specific modifications of the calcite isotopic signal, the well-characterized portions of these records can provide observational constraints for evaluating the modeled $\delta^{18}O_p$ response over the KP.

Formatted: Subscript

2.2 Isotope-enabled model simulations

Deleted: The age models of these speleothems and the associated $\delta^{13}C_{sp}$ records were previously discussed, and information on sampling and measurement of stable isotopes can be found in Jo et al. (2010, 2014). Further details and the periods covered by the $\delta^{18}O_{sp}$ records, as well as other proxies used in this study, are provided in the supplementary Table S1.

For this study, we performed a series of fully coupled paleoclimate simulations with the iCESM1.2 (Brady et al., 2019), using a model resolution of approximately 1.9°x2.5° in the atmosphere and land and 1°x1° in the ocean and sea ice, respectively, providing simulated precipitation oxygen and hydrogen isotopes ($\delta^{18}O$ and $\delta^{2}H$) (Brady et al., 2019; Hu et al., 2019; Tabor et al., 2018). We also combine simulated precipitation stable-isotope data to examine precessional variations in precipitation d-excess ($\delta^{2}H - 8\times\delta^{18}O$) (Dansgaard, 1964). To validate our iCESM1.2 present-day (iCESM-PD) simulations, we have used the available IAEA Global Network of Isotopes in Precipitation (GNIP) datasets for the Asian domain (Accessible at https://nucleus.iaea.org/wiser), published precipitation isotope records (Sinha et al., 2019), and data from the isotopes-incorporated Global Spectral Model – isoGSM2 (Yoshimura et al., 2008).

Deleted: -scale

First, we conducted an idealized transient simulation covering the orbital forcing history of the past 130,000 years (iCESM-130ka), using fixed pre-industrial conditions of greenhouse gas (GHG) concentrations, ice sheets, and bathymetry. The transient simulation employs an orbital temporal acceleration (Lorenz and Lohmann, 2004a; Timmermann et al., 2007) factor of 100, consistent with previous studies, which compresses the 130,000-year forcing history into 1,300 model years. The acceleration choice is justified by the fact that we focus here on atmospheric processes primarily controlled by changes in land and ocean surface temperatures, with adjustment timescales that are orders of magnitude faster than the precessional cycle forcing. In our 130 ka-orbitally forced iCESM1.2 simulation, we analyzed the spatiotemporal patterns of annual-mean anomalies of precipitation amount and $\delta^{18}O_p$. We further compared our simulated precipitation patterns with the transient CESM1.2 simulation over the past three million years (CESM-3Ma) (Timmermann et al., 2022; Yun et al., 2023), which was forced by time-varying orbital, GHG, and ice-sheet forcings. CESM-3Ma simulation uses a lower horizontal resolution (3.75° in the atmosphere and 3° in the ocean), and an orbital acceleration of only 5, but does not include isotopes.

Deleted: realistic

Next, we performed model sensitivity experiments with iCESM1.2 to evaluate the equilibrium climate responses to maximum (P_{max}) and minimum (P_{min}) precession conditions (iCESM-P_{max} and iCESM-P_{min}). These 100-year-long fully coupled time-slice sensitivity experiments branch off from year 900 of a 1,000-year-long iCESM-PD control experiment. The two idealized simulations use a high eccentricity (Berger and Loutre, 1991) of 0.0493 to amplify the precessional effects. The simulations reach a quasi-equilibrium state for important atmospheric variables within 100 years. Much of our analysis from these two simulations is based on the June-July-August (JJA) seasonal averages of the last 40 model years. Furthermore, we compared iCESM P_{min} and P_{max} precipitation and circulation patterns with ultra-high-resolution simulations (1/4° in the atmosphere and 1/10° in the ocean) conducted for Marine Isotope Stages (MIS)-5d (115 ka) and MIS-5e (125 ka) using the CESM1.2 (Chu et al., 2020; Huang et al., 2021; Raavi et al., 2023; Wengel et al., 2021) (hiresCESM-5d and hiresCESM-5e). This analysis provides further insights into the robustness of our results, enabling a more nuanced characterization of regional aspects.

To quantify the KP precipitation and $\delta^{18}O_p$ responses to the P_{min} and P_{max} conditions, we performed water-tagging experiments using the iCESM to track changes in source regions and their relative contributions to the KP. The experiments were conducted using orbital parameters corresponding to 124 ka (Pmin) and 119 ka (Pmax), along with current atmospheric and

Deleted:

oceanic conditions (including the initial isotopic composition) derived from the iCESM-PD simulation. We tag a total of 14 boxes (7 each over land and Ocean), based on the major contributors to the Asian region (Hu et al., 2019). The box latitude and longitude were chosen following Wen et al. (2024), although we have excluded regions from the calculations with minimal contribution (< 10 %) to the total rainfall and no effect on the anomalous $\delta^{18}O_p$. The regional pattern of the simulated $\delta^{18}O_p$ is determined by the $\delta^{18}O$ of the vapor from the tagged regions, followed by hydrological processes and rainout history (Tabor et al., 2018). Each tagging experiment was conducted over 40 model years, with the mean values from the last 20 years (both summer and annual) used for analysis. Further information on the tagging experiment is provided in the supplementary material (Section S1).

3 Results and Discussion

3.1 Precipitation and $\delta^{18}O$: Model and Proxies

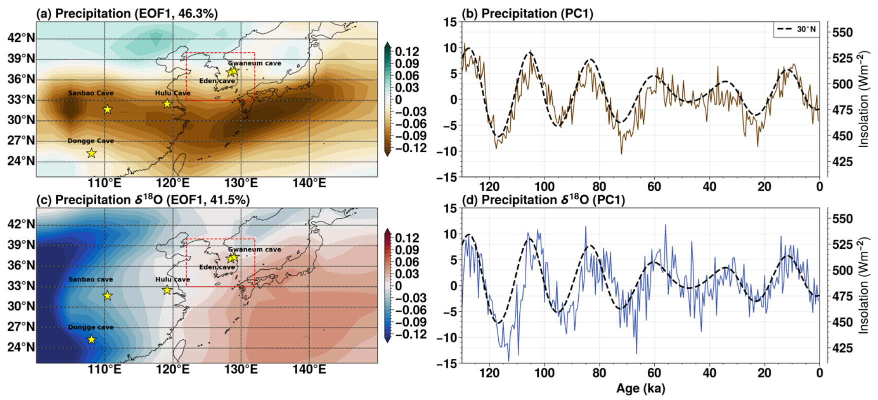

__Figure 1:__ First empirical orthogonal function (EOF1) and corresponding principal component (PC1) of precipitation (a, b) and precipitation-$\delta^{18}O$ (c, d) annual anomalies for the selected Eastern Asian region (22-45°N, 100-150°E). Annual anomalies were calculated by subtracting the long-term annual mean value (i.e., the climatological annual mean) from each annual mean. Annual means were obtained by averaging the monthly simulated values. Korean caves and cave locations for the China composite record are marked with yellow stars in (a) and (c).

Formatted: Font: Bold

Deleted: *annual mean*

Deleted: *anomalies are calculated for Eastern Asia using the 130ka orbitally forced transient iCESM simulation.*

Deleted: *by*

Deleted: *,*

A red dashed box marks the Korean Peninsula (KP) region. The black dashed curve in (b, d) represents summer insolation at 30°N.

To extract the dominant modes of variability in Eastern Asia, we used precipitation amount and $\delta^{18}O_p$ annual anomalies from the transient iCESM-130ka simulation. We calculated the first Empirical Orthogonal Function (EOF1) and the corresponding principal component (PC1) time series for the selected Eastern Asian region (22-45°N, 100-150°E), including eastern China, the KP, and Japan (Fig. 1). The leading EOF of annual mean precipitation variability exhibits a north-south dipole in the selected EASM domain (Fig. 1a), characterized by strong precessional variability and correlating with the NHSI at 30°N (Fig. 1b). The precipitation anomalies associated with the change in boreal summer insolation exhibit the strongest signal in an east-west elongated structure between 25°N and 35°N. For northern-hemisphere summer perihelion conditions (low precessional index), this area is characterized by anomalously dry conditions, whereas for northern-hemisphere summer aphelion conditions (high precessional index), it is characterized by anomalously wet conditions (Fig. S2). Most notably, Korea lies on the nodal line of the precipitation dipole pattern, suggesting a weak annual-mean precession signal over the KP (Fig. 1a). A similar precipitation pattern also emerges for the CESM-3Ma transient simulation (Yun et al., 2023) over the study area (Fig. S3), indicating that the effects of GHGs and ice sheet forcing are relatively minor in driving the EASM spatial precipitation patterns on precession scales. However, in this case, the nodal line lies slightly south of the KP. The ultra-high-resolution simulations confirm the overall large-scale response pattern in summer precipitation to changes in the precessional index, albeit with somewhat drier conditions over the KP, relative to the coarser-resolution CESM-3Ma and iCESM-130ka simulations (See comparisons in Fig. S2).

Contrasting the meridional dipole in precipitation, the leading mode of $\delta^{18}O_p$ variability exhibits an east-west (zonal) dipole pattern over our selected study region (Fig. 1c). The $\delta^{18}O_p$

Deleted: ,

Deleted: w

Deleted: calculate

Deleted: -scale

dipole, which is characterized by relative ^{18}O-depletion (enrichment) for western (eastern) Asia during Northern Hemisphere summer perihelion, has previously been presented as a notable feature over the broader Asian summer monsoon region on precession scales (Wen et al., 2024). In the western part of this dipole (China), we observe pronounced precessional timescales $\delta^{18}O_p$ signals; in the eastern part (Japan, Korea, and nearby seas), we generally find weaker variability that is antiphase with the west (Fig. 1c and Fig. 1d). For the KP region, the simulated precessional signal in $\delta^{18}O_p$ is strongly suppressed (similar to the rainfall pattern), and no distinct precession cyclicity is evident in the simulated time series (Fig. S4).

The near absence of precessional variability in hydroclimate predicted by the models can now be tested using our speleothem isotope data from the KP (Fig. 2a). The Korean speleothem stable carbon isotope ($\delta^{13}C_c$) records aligns well with Chinese $\delta^{18}O_c$ during overlapping periods (Fig. 2b), and the growth frequency of Korean speleothems exhibits clear signals that correspond to orbital-timescale hydrologic changes (Jo et al., 2014). However, Korean stalagmites records show no apparent precessional signal (Fig. 2b). The weak covariation between $\delta^{13}C_c$ and $\delta^{18}O_c$ (ED1, $R^2 = 0.16$, $p < 0.01$; GE1, $R^2 = 0.04$, $p = 0.02$) suggests that kinetic effects are unlikely to be the primary control on their variability. Moreover, the precessional-scale variability in the Korean $\delta^{18}O_c$ records is strongly suppressed relative to the relatively pronounced (~4‰) variability observed in the Chinese composite $\delta^{18}O_c$ record (Fig. 2b). This observational evidence is consistent with the muted response of $\delta^{18}O_p$ over the KP to precessional forcing in the simulations (Fig. 1c). This raises the question of which physical processes govern the Korean $\delta^{13}C_c$ on precessional timescales. Previous studies from the KP (Jo et al., 2010, 2011, 2014) suggested that glacial-interglacial changes in $\delta^{13}C_c$ could be related to summer-temperature and rainfall-driven anomalies in terrestrial productivity. However, a more detailed investigation of the underlying processes driving precessional-scale variations in $\delta^{13}C_c$ is beyond the scope of our comprehensive water-isotope analysis of the KP.

Deleted: n
Deleted: h
Deleted: -scale
Deleted: sp
Deleted: correspond well with the Chinese $\delta^{18}O_{sp}$ records
Deleted: blue and gray curves, respectively,
Moved down [2]: This observational result is consistent with the muted response in simulated $\delta^{18}O_p$ in the KP region to precessional forcing (Fig. 1c).
Deleted: $\delta^{18}O_{sp}$
Deleted: red curves,
Formatted: Subscript
Formatted: Subscript
Moved (insertion) [2]
Deleted: This observational result is consistent with the muted response in simulated $\delta^{18}O_p$ in the KP region to precessional forcing (Fig. 1c)
Deleted:
Deleted: sp
Deleted: a
Deleted: precessional-scale
Deleted: sp
Deleted: (Jo et al., 2014)sp

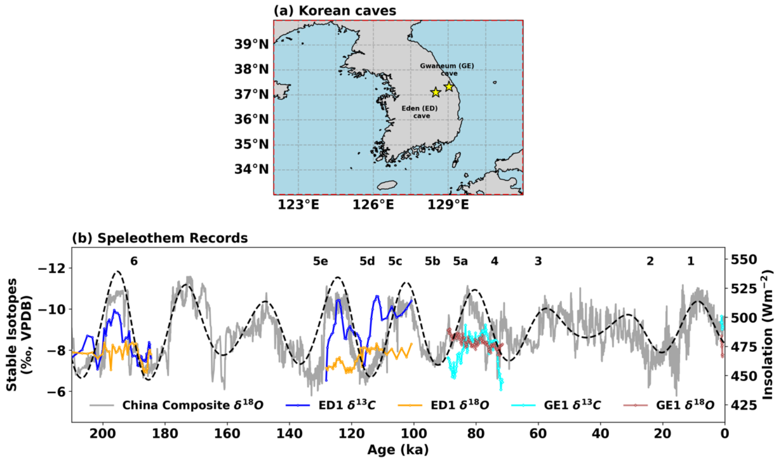

Figure 2: *Korean Peninsula (red box, Figure 1) with Korea cave locations (a). Speleothem stable isotope records (δ^{13}C and δ^{18}O) from Korean caves (Gwaneum (GE) cave and Eden (ED) cave) stalagmites (GE1 and ED1) and the Chinese caves composite-δ^{18}O record comparison (b). The marine isotope stage (MIS) is indicated above the curves in (b). The black dashed curve in (b) represents summer insolation at 30°N.*

According to the transient iCESM-130ka and CESM-3Ma simulations, precipitation over Eastern Asia (Fig. 3b) exhibits precessional signals, which are out of phase with insolation. It is important to note that simulated precessional scale precipitation suppresses during glacial maxima in eastern Asia, documenting the influence of the 80-120 kyr eccentricity forcing on the amplitude modulation of precession (Fig. 3a and Fig. 3b). There are several East Asian hydroclimate proxies, such as ^{10}Be in loess from central China (Beck et al., 2018), pollen records from Japan (Hayashi et al., 2017, 2021; Tarasov et al., 2011) (Fig. 3c), and total nitrogen content in Lake Biwa (Iwamoto and Inouchi, 2007), which support and demonstrate the above-mentioned features in regional-simulated precipitation. Speleothem records from Japan (Kato et al., 2021; Mori et al., 2018) lack sufficient data points within the 0-130ka simulated period, and the intermittent time span does not encompass high-insolation periods, which would be necessary to validate the simulated isotopic composition. Some mismatches between the pollen records and the model occur during MIS11 and low-CO_2 conditions,

Formatted: Font: Bold

Deleted: *Korean peninsula (red box, Figure 1) with Korea cave locations (a). Speleothem records (δ^{13}C and δ^{18}O) from Korean caves (Gwaneum (GE1) cave and Eden (ED1) cave) and the Chinese caves composite record (δ^{18}O) comparison (b). The marine isotope stage (MIS) is indicated above the curves in (b). The black dashed curve in (b) represents summer insolation at 30°N.*

suggesting that vegetation dynamics in the region may, in part, be driven directly by CO_2, either through temperature or the CO_2 fertilization effect. However, uncertainties in the chronology of the palynological reconstruction preclude a definitive conclusion at this time. Moreover, the simulations indicate a stronger 41ka obliquity signal, particularly during periods of low eccentricity, which seems absent in the paleo proxy records (Fig. 3b).

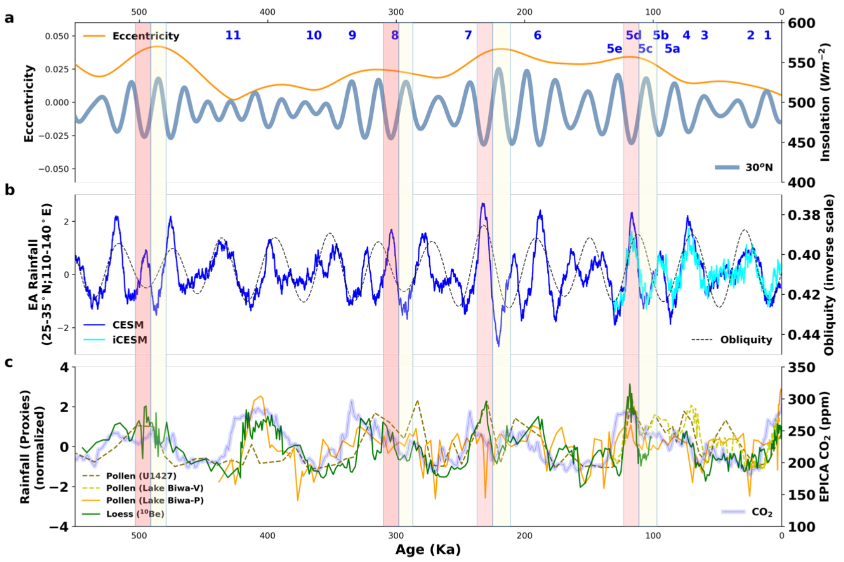

__Figure 3:__ Comparison of simulated Eastern Asian (EA) rainfall from the climate model simulations with prominent precipitation proxy records from the region over the last 550 ka. Summer Insolation (30 °N) and eccentricity (high eccentricity and low/high insolation highlighted with pink/yellow bars) (a). Rainfall (mm/day) from iCESM (this study) and CESM 3Ma simulations, along with obliquity (b). Loess ^{10}Be (central China) and EASM rainfall (Beck et al., 2018), along with CO_2 and palynological (Japan) rainfall reconstructions using the Lake Biwa pollen records (c). Lake Biwa-V (Hayashi et al., 2017) is based on vegetation response, and Lake Biwa-P (Tarasov et al., 2011) is based on the modern analogue technique. The marine isotope stage (MIS) is indicated above the top panel curves. For records' references, see Table S1. It should be noted that the Chinese ^{10}Be record has been plotted after shifting the age by -6ka (see Section S2), which then aligns well with other regional proxies (c) and model-simulated precipitation (Fig. S5).

Deleted: *4*

3.2 Precession versus EASM atmospheric circulation

As discussed in the previous section, under low precession conditions, a region of low precipitation in the eastern EASM domain zonally extends from KP across southern Japan into the central North Pacific. Our simulation shows that the region of low precipitation is co-located with an anomalously high sea level pressure (SLP; contour lines, Fig. 4a) and suppression of atmospheric convection (Fig. S6c, contour), in concordance with the intensification of the anomalous WNPSH (geopotential height, Fig. S6c). Supporting evidence comes from an integrated moist static energy budget analysis by Wen et al. (2024), which showed that the reduction in rainfall is linked to descending air motion. Our simulated precipitation pattern, meridional and zonal wind components, and strength of anomalous WNPSH are well supported by the difference of the hiresCESM-5e and hiresCESM-5d experiments (Fig. 4b and Fig. S6), even though the anomalies over the KP are slightly stronger compared to the ~2 degree resolution iCESM.

Deleted: 5

Deleted: 5

Deleted: 5

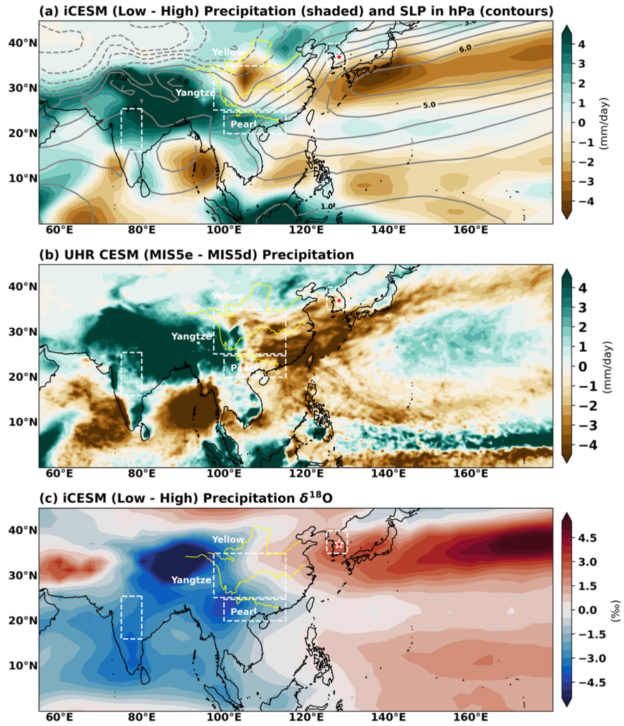

Figure 4: *Difference between precession minimum (Low) and maximum (High). Composites of summer mean precipitation (shaded) and sea level pressure (SLP, contour), from iCESM1.2 (a). Same as (a) with CESM Ultra High Resolution (UHR) simulation for MIS5e and 5d (b), and summer mean precipitation-$\delta^{18}O$, from iCESM1.2 (c). The dashed boxes shown are used to extract 130 ka time series from the model simulations: India, central China, South China, and Korea (left to right in increasing longitude order). The yellow curves on the map indicate major rivers in China. The red star represents the Korean cave region.*

In addition, the simulated western branch of the anomalously strong WNPSH (Fig. S6c, f) might help transport more moisture from the Pacific Ocean toward northern China and the northern part of KP, resulting in regional positive precipitation anomalies in the model. The rainfall pattern corresponds to an overall weakening and a slight northward shift of the Korean and Japanese summer monsoon systems, specifically the Changma and Meiyu-Baiu fronts, respectively. On the other hand, the KP hydroclimate reconstructed from speleothem proxies (viz., growth frequency) suggests signals of a wetter climate during interglacial periods (Jo et

Deleted: 3
Deleted: a
Deleted: d

al., 2014), which are characterized by northern hemisphere summer perihelion. These observations highlight the importance of considering speleothem-specific characteristics, including site location, local orography, cave processes, and chronological precision, when comparing individual speleothem records with spatially resolved simulations, particularly for distinguishing hydroclimatic changes between closely spaced intervals such as MIS 5e and MIS 5d. It is worth noting that the Korean caves are primarily located in the mountainous Gangwon-do region of South Korea and range in altitude (Jo et al., 2014). It is possible that orbital forcing may also influence the precipitation intensity and the extent of the nodal line, relative to local topographic features (Fig. 4b). Thus, the apparent contrast between the speleothem growth-frequency records and the simulated muted response over the broader KP region may partly reflect spatial heterogeneity in the regional hydroclimate response.

We further explored the mechanisms underlying the precessional-scale muting of precipitation and $\delta^{18}O$ for the KP and other parts along the nodal line, both for summer (JJA) and annual-mean conditions. Using the water tagging method, we estimated the contributions from different moisture sources to precipitation and $\delta^{18}O_p$ at the KP in JJA (Fig. 5). The Pacific Ocean transports more moisture to the KP region during the northern hemisphere summer perihelion (Fig. 5a). This anomalous moisture predominantly originates from the subtropical North Pacific (SNP, 0.40 mm/d) due to the strengthening and northwest shift of the NWPSH. Land moisture (Fig. 5b) from the East Asia region also contributes to the anomalous P_{min} precipitation over the KP in JJA (EAS, 0.11 mm/d). However, during P_{min} less moisture from the northern North Pacific (NNP, -0.15 mm/d) and the equatorial Indian Ocean (EQI, -0.09 mm/d) arrives in KP, which compensates the increase with a small cumulative change in summer precipitation of 0.28 mm/d as a result. The annual-mean KP precipitation anomaly between P_{min} – P_{max}, shows only a small change, ranging from 0.023 (SNP) to -0.15 mm/d (EAS) in terms of moisture contributions (Fig. S7, Table S2).

Deleted: for the precessional muting of precipitation and $\delta^{18}O_p$ for the KP and other parts along the nodal line, both for summer (JJA) and annual mean

Deleted: -isotope

Deleted: 6

JJA $\delta^{18}O_p$ over the KP, will be determined both, by regional rainfall and water vapor transport contributions from the different source regions. Using the isotope tagging method, we calculated summer precipitation-weighted $\delta^{18}O_p$ values (Sect. S1 and Table S2) at the KP (inset, Fig. 5). We find that the moisture transported from the SNP oceanic region to the KP is characterized by anomalously high $\delta^{18}O$ values (i.e., enriched in ^{18}O) during P_{min} relative to P_{max} by +0.22‰, with EAS land moisture also contributing higher $\delta^{18}O$ values ($P_{min} – P_{max}$ = +0.31‰). However, the moisture transported from the distant Indian Ocean (EQI) and the land (SAS) regions shows a compensating effect, with lower $\delta^{18}O$ values (EQI + SAS = -0.38‰). Combining the positive $\delta^{18}O$ contributions from the SNP and EAS regions with the negative contributions from the EQI and SAS regions results in a small net increase in $\delta^{18}O$, corresponding to higher JJA $\delta^{18}O_p$ values (+0.22 ‰) over the KP during P_{min}. On annual timescales (inset, Fig. S7), this compensation is even more pronounced, leading to a slight net depletion in ^{18}O (lower in $\delta^{18}O_p$ values) over the KP by -0.10‰ (P_{min} - P_{max}). Furthermore, the tagging experiment reveals that, for annual means, the Indian region plays a negligible role in precessional-scale changes in precipitation and $\delta^{18}O_p$ over the KP (Fig. S7, Table S2).

Deleted: Using the tagging methods and calculating summer precipitation-weighted $\delta^{18}O_p$ values (Sect. S1 and Table S2) at KP (inset, Figure 5), we find that the moisture transported from the SNP oceanic region to the KP is anomalously enriched in P_{min} relative to P_{max} (+0.22‰), with additional contributions also from EAS land moisture ($P_{min} – P_{max}$ = +0.31‰). However, the transport of moisture from the distant Indian Ocean (EQI) and the land (SAS) regions shows a compensating effect (EQI + SAS = -0.38‰). Combined the SNP and EAS effects (enrichment) and the EQI and SAS contributions (depletion) result in a small net anomalous enrichment of $\delta^{18}O_p$ (+0.22 ‰) in JJA over KP during P_{min}. On annual timescales (inset, Fig. S6), the compensation is even more pronounced, leading to a small net depletion of $\delta^{18}O_p$ over the KP region by -0.1‰ (P_{min} - P_{max}).

Deleted: 6

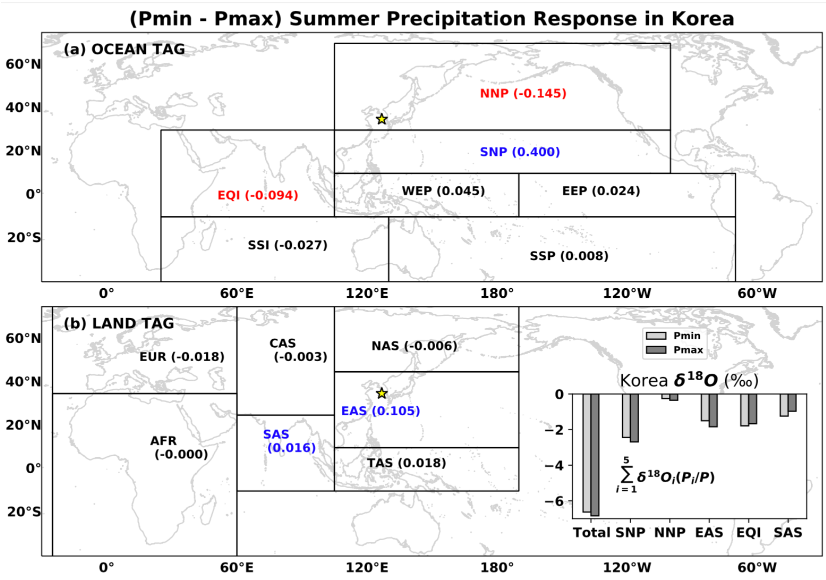

Figure 5: *Differences in average summer (Jun-Aug) precipitation (mm/day) on the Korean Peninsula between Pmin and Pmax from various moisture sources over (a) ocean and (b) land. Colored text refers to the major contributors (mean-state) to the Korean Peninsula (blue-positive and red-negative for Pmin-Pmax), as shown in Table S2, which was considered in the total calculations. Inset plot (lower right): the summer precipitation-weighted $\delta^{18}O$ in Korea from major and nearby source contributors from Land (EAS, SAS) and the Ocean (SNP, NNP, EQI). Korea is marked by a yellow star. See the supplementary material for the acronyms.*

Overall, there is a tug-of-war between contributions from different oceanic and continental regions to KP $\delta^{18}O_p$, leading to the muting of the precessional signal. For instance, the anomalous WNPSH leads to a westward (eastward) shift of the ISM branch towards northern China under low (high) precession conditions, as documented by an analysis of the vertically integrated moisture transport (VIMT, Fig. S8). The schematic in Figure 6 summarizes these findings by highlighting changes in circulation patterns and simulated $\delta^{18}O_p$ values for P_{min} and P_{max} conditions.

Deleted: *p*

Deleted: 7

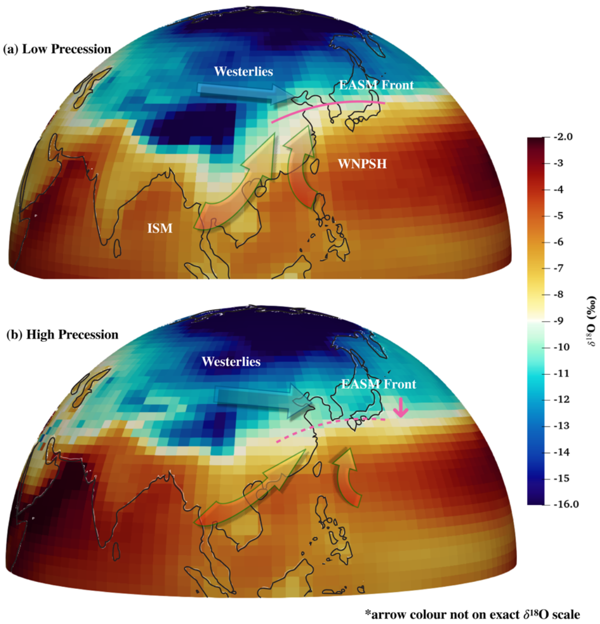

Figure 6: *Schematics of precession effects on summer East Asian monsoon circulation and spatial distribution of precipitation-$\delta^{18}O$ (blue to dark orange: depleted (low $\delta^{18}O$) to enriched (high $\delta^{18}O$) in ^{18}O in relative to low and high precession conditions). The thickness of the arrows represents the strength of the circulation systems. The solid and dashed pink lines indicate the location of the EASM front. (a) In the low precession case, ISM strengthening (a more southerly component), Westerlies (northward), and WNPSH (northwest) result in low (high) $\delta^{18}O_p$ over India to northern China (eastern Asia). The solid pink line indicates the EASM front location. (b) For the high precession case, the combined effects of the weakening of the ISM (more northeast component), the southward migration of the Westerlies, and the eastward movement of the WNPSH result in suppressed transport of Pacific moisture into the eastern domain of the EASM, result in high $\delta^{18}O_p$ across India to East Asia, however leading to relatively low $\delta^{18}O_p$ in eastern Asia. The interactions between two circulation systems (ISM and EASM) and the Westerlies create a nodal zone, which includes the Korean Peninsula (KP).*

Formatted: Font: Bold

Formatted: Superscript

Given the oceanic-continental moisture contributions to the orbital-scale characteristics of precessional-scale changes in KP hydroclimate, we anticipate that the dynamics will also be well captured in d-excess, which reflects the source region (Araguás-Araguás et al., 2000; Jouzel et al., 2013; Pfahl and Sodemann, 2014) and evaporative conditions (Masson-Delmotte et al., 2005; Uemura et al., 2008) of the moisture source. Like the d-excess seasonal variations, to some extent, can serve as an analog for precessional changes, as precessional forcing oftentimes modulates the amplitude of the seasonal signals in precipitation and isotopic composition, due to the strength and position of atmospheric circulation (Bosmans et al., 2018). As such, we examined d-excess variations on precessional timescales in our iCESM simulations.

3.3 Deuterium excess in simulations

d-excess, a secondary parameter derived from stable water isotopic ratios, provides additional insights into hydrological processes. Non-equilibrium conditions can lead to enrichment of ^{2}H in the less stable phase (e.g., the gas phase) due to the higher diffusivity of hydrogen isotopes relative to oxygen. For instance, during evaporation from the ocean surface, the strong gradient in relative humidity accompanied by strong winds leads to higher d-excess in the vapor (Craig and Gordon, 1965; Uemura et al., 2008). It has been suggested that climatic influences on relative humidity, mediated by changes in atmospheric circulation, are captured in the d-excess proxy in precipitation-based paleoarchives (Pfahl and Sodemann, 2014) (e.g., ice core, speleothem). Studies have shown that the d-excess in paleowater can, in fact, be recovered from fluid-inclusion data in certain speleothems (Held et al., 2025; Matthews et al., 2021).

Deleted: speleothem
Deleted: fluid
Deleted: inclusion
Deleted: data

The precipitation d-excess is sensitive to various hydrological processes between the "source" and the "sink" (Xia et al., 2023), such as evaporation at the moisture source location (Craig and Gordon, 1965; Merlivat and Jouzel, 1979), moisture recycling from the land (Gat, 1996; Gat et al., 1994), raindrop evaporation (Risi et al., 2008; Stewart, 1975), and Rayleigh distillation (Xia et al., 2023). On precessional timescales, one crucial parameter is the near-surface relative humidity (Rh_s) at the source location. Over the tropical monsoon region, Rh_s changes may occur mainly in conjunction with wind anomalies, as the annual mean surface temperature changes are quite small on precession scales (Clement et al., 2004). We have analyzed the characteristics of simulated Rh_s at plausible source locations and d-excess variations at the sinks. The spatial pattern and gradient of surface relative humidity over the Asian region are reasonably well captured in the present-day simulation (Fig. S9). Brady et al. (2019) reported that the d-excess values simulated by iCESM1 exhibit a positive median bias of 3.3‰ and a poor correlation with GNIP observations. Our reinvestigation of simulated d-excess in the Asian region for present-day conditions shows that GNIP and model data align reasonably well (Fig. S10). A closer look at Fig. 4(b) in Brady et al. (Brady et al., 2019) supports this conclusion. For the Asian region, we found good agreement ($r = +0.52$, $p < 0.01$) between the annual mean d-excess in GNIP observations and our iCESM-PD simulation (Fig. S11), with a smaller median bias of +1.75‰, compared to the 3.3‰ global mean bias. Moreover, the strong seasonality in the observed (GNIP) d-excess for East Asia, specifically for north and eastern Asian sites, is well captured in iCESM-PD (Fig. S12), which is crucial in the current context because precessional shifts are likely to influence the amplitude of the seasonal cycle, rather than the annual mean.

Deleted: 8

Deleted: 9

Deleted: 0

Deleted: 1

To refine our interpretation of d-excess as a proxy for precessional signals over Asia, we further investigate Rh_s variability in the Asian monsoon oceanic source domains, including the Indian and Pacific Oceans. In the calculated EOFs for the Rh_s from the iCESM-130ka simulation, EOF2 represents precessional-scale changes (Fig. 7). Over the southeast Indian Ocean and northwest Pacific Ocean (rectangular boxes in Fig. 7), we observe strong precessional-scale variability in Rh_s (Fig. 7b), with an amplitude change of approximately 3%-4% (Fig. 7c, d). The chosen blue and red boxes, which exhibit strong out-of-phase variability (Fig. 7a), respectively, closely correspond with the dominant moisture source regions to the South Asian (Tabor et al., 2018) and Eastern Asian (Wen et al., 2024) monsoon regions under P_{min} climate (black dashed boxes, Fig. 7a). Subsequently, our results indicate that the South Asian and East Asia (mainly Northeast China) continental domains also exhibit a substantial precessional-scale variability in Rh_s (Fig. S13a, b), with an amplitude of about 10% change and in phase with the NHSI (Fig. S13c, d).

Deleted: 2

Deleted: 2

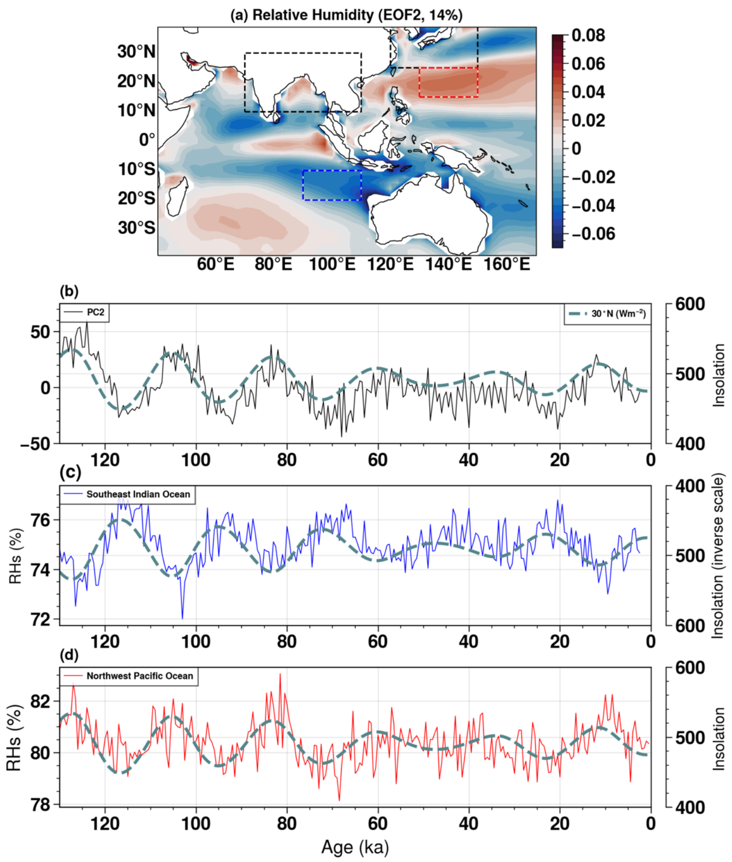

Figure 7. *Second empirical orthogonal function (EOF2, a) and corresponding principal component (PC2, b) for the summer mean surface relative humidity for the 130ka transient simulation on iCESM1.2. Temporal evolution of surface relative humidity over oceanic source regions, Southeast Indian Ocean: blue curve (c) over blue dashed box (a); and Northwest Pacific Ocean: red curve (d) over red dashed box (a). The black dashed boxes represent the South Asian summer monsoon and the eastern extent of the EASM region (a). The dashed curve represents summer insolation at 30°N.*

Moreover, our results show that the P_{min} and P_{max} conditions exhibit opposite signals in precipitation d-excess values between South Asia and East Asia (Fig. 8a). The d-excess is high over India and low over central China for P_{min}. Specifically, in the KP, d-excess is low (high) for high (low) NHSI. It should be noted that the KP d-excess differences for $P_{min} - P_{max}$ are predominantly from the changes during the summer season; however, the Indian region's d-excess values are higher throughout the year for P_{min} relative to P_{max} (Fig. S14). Our tagging results also show that transported moisture from the Pacific Ocean and the East Asia continental regions contributes to lower d-excess at KP under P_{min} conditions (Fig. S15), likely due to relatively higher humidity over the source regions (Fig. 7d and Fig. S12d). To evaluate the Rh_s and d-excess relationship quantitatively, the translation of the source region's Rh_s change to the sink's precipitation d-excess has been estimated from the iCESM-130ka simulation. A regional Rh_s regression on d-excess shows about a 0.3-0.4‰ increase in summer precipitation d-excess values over South Asia with a 1% decrease in source region (southeast Indian ocean) Rh_s (i.e., Δ(d-excess)/ΔRh_s = ~ -0.4) (Fig. S16a). And a 1% increase in Rhs in the northwest Pacific Ocean can cause a 0.7-0.8‰ decrease in summer precipitation d-excess across Eastern Asia (i.e., Δ(d-excess)/ΔRh_s = ~ -0.8) (Fig. S16b).

Deleted: 3

Deleted: 4

Deleted: 5

Deleted: 5

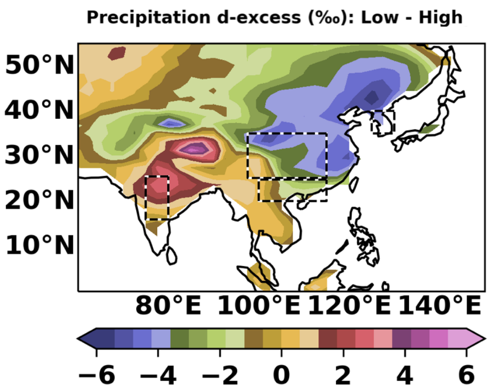

Figure 8: *Precipitation d-excess for Low (P_{min}) - High (P_{max}) precession conditions. Black dashed boxes represent regions: India, Central China, South China, and Korea (left to right), used to extract the time series from the iCESM1.2 simulations.*

3.4 Pan-Asian monsoon context

In this section, we refine our understanding of speleothem records from the KP in the broader context of hydroclimate changes across South to Eastern Asia in our transient simulation (Fig. S4). The iCESM-130ka simulation shows dominant anti-correlated precessional variability in precipitation between India (representative of Southern Asia) and central China (Fig. 9a and Fig. 9e). Furthermore, the amplitude of this variability is stronger (weaker) for high (low) eccentricity values, such as during MIS 5a-e and MIS3. On the other hand, precessional-scale variability in simulated KP precipitation, as well as in parts of southern China, is strongly muted (Fig. 9c and Fig. 9g), as discussed above. Moreover, over the KP, we found that precipitation exhibits an 11-kyr higher-order precessional harmonic, for instance, during MIS 5d and MIS 4 (Fig. 9g). This signal likely arises from the nonlinearity of the moisture transport equation, which multiplies precessional-scale winds with precessional changes in moisture, leading to semi-precessional variability.

Deleted: 16

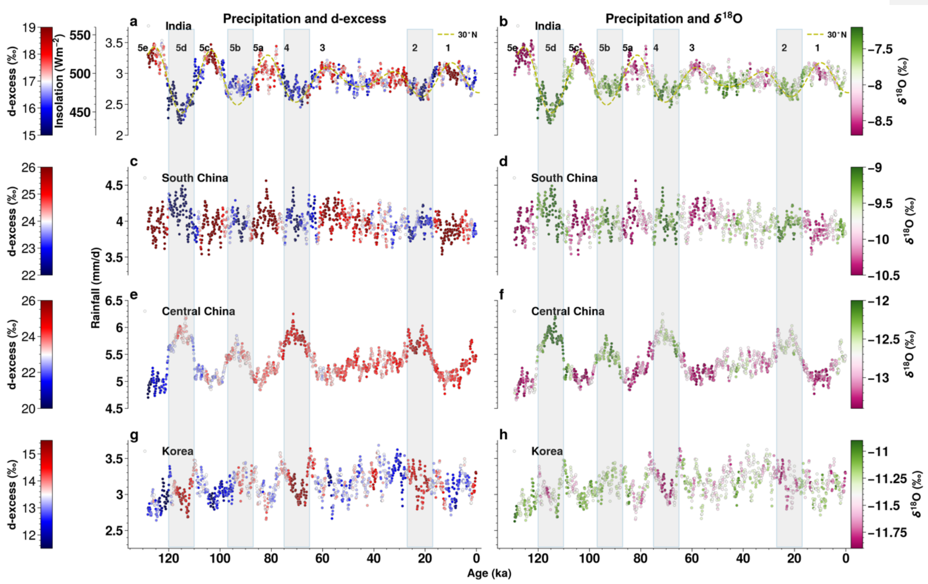

Figure 9: *Simulated annual mean variations in precipitation (dots) for the last 130ka from an orbital forced transient simulation conducted with iCESM1.2 for India (a,b), South China (c,d), central China (e,f), and Korea (g,h) (see selected region boxes in Figure 8) in addition, colors of dots show precipitation-$\delta^{18}O$ (pink to green, right panel) and d-excess (blue to red, left panel) changes. Low insolation periods are marked by gray bars. The marine isotope stage (MIS) is indicated above the top panel curves.*

In the Indian region, apart from the strong precessional signals in precipitation, we see precessional variability in d-excess and $\delta^{18}O_p$, with high (low) d-excess and depleted (enriched) $\delta^{18}O_p$ values for high (low) insolation (Fig. 9a and Fig. 9b). Here, the change in d-excess values is predominantly controlled by the surface conditions at the ISM moisture source region, that is, high and low Rh_s values for low and high precession conditions, respectively, as discussed above. In central China, $\delta^{18}O_p$ varies in phase with the anomalies over India (Fig. 9b and Fig. 9f). However, their d-excess variations are essentially anti-correlated (Fig. 9a and Fig. 9e), in particular for MIS5e and 5c, reflecting the complex interplay between the Indian and Pacific Ocean moisture sources and continental moisture effects. Our results support the previously suggested role of the ISM branch in controlling precipitation isotopic ratios across China (see supporting Fig. S4a and Fig. S4b). Furthermore, we observe that KP precipitation and $\delta^{18}O_p$ exhibit little precessional variability due to the compensating effects described above. In contrast, d-excess over the KP shows a more pronounced precessional signal (Fig. 9g). This d-excess variability responds to the balance between oceanic and continental moisture transport and changes in the surface conditions of source regions (i.e., Rh_s) on precessional scales. Moreover, the KP d-excess precessional-scale variability is a unique feature as compared to other Eastern Asian regions, with high values occurring during MIS 5d, b, 4, and 2. The positive feedback (kinetic effect) to the vapor d-excess could be even stronger for P_{max} relative to P_{min} when dry/cold winds pass over the ocean (Yoshimura and Ichiyanagi, 2009) (e.g., the Yellow Sea).

4 Summary and concluding remarks

Our study focuses on the muted precessional-scale hydroclimate variations in the KP region, as observed in our transient climate model simulations and $\delta^{18}O_c$ records from South Korean caves. The muting of the $\delta^{18}O_p$ signal can be attributed to compensating effects between oceanic and continental moisture sources. We further explored how the KP hydroclimate is linked to large-scale pan-Asian atmospheric variability. Our study illustrates that even along the nodal line of the oxygen isotope dipole pattern, where $\delta^{18}O_c$ and the iCESM simulation indicate weak precessional variability in $\delta^{18}O_p$, the d-excess may still contain important precessional signals, which are associated with large-scale changes in Pacific, Indian, and continental moisture source region conditions, driven by the precessional changes in the Asian summer monsoon circulation and in the intensity of the WNPSH. Therefore, we advocate validating model simulations using speleothem fluid inclusions (paleowater) to shed more light on regional rainfall variability and large-scale atmospheric circulation changes across multiple timescales, even in regions like the KP where oxygen isotope signals are muted.

Our simulations exhibit another interesting feature that has not previously been recognized: simulated Korean precipitation shows evidence of semi-precessional hydroclimate variability. A few studies have suggested that such semi-precessional signals may result from a response to solar insolation in low latitudes, modulating the EASM. Other potential mechanisms include combination tones of the moisture transport, emerging from the product between precessional signals in specific humidity and atmospheric advection. However, the underlying mechanism for the semi-precessional variability over the KP remains unclear and may require further investigation.

The present study highlights the importance of a multi-proxy approach, utilizing additional speleothem proxies, such as trace elements, $\delta^{13}C$, and growth rate or frequency, in conjunction

Deleted: $\delta^{18}O_{sp}$

Deleted: $\delta^{18}O_{sp}$

with fluid inclusions (d-excess). While reconstructions of paleo-water d-excess provide valuable information on past moisture source conditions and evaporation processes, suitable fluid inclusions are not always preserved or available for analysis. In such cases, oxygen-17 excess (^{17}O-excess) measured directly from speleothem calcite and is not sensitive to temperature variations, offers a promising complementary proxy (Sha et al., 2020, 2023). Future paired measurements of $\delta^{18}O$, d-excess, and ^{17}O-excess in speleothems could therefore provide a powerful framework for testing the circulation and moisture-source mechanisms inferred in this study. In addition, multiproxy speleothem data, along with data from marine and lacustrine archives, may provide further insights into regional hydroclimatic variability in the EASM region, and help reconcile different hydroclimatic records and elucidate their underlying mechanisms.

Deleted: The present study highlights the importance of a multi-proxy approach, utilizing additional speleothem proxies, such as trace elements, $\delta^{13}C$, and growth rate or frequency, in conjunction with fluid inclusions. These proxies, along with data from marine and lacustrine archives, may provide further insights to help reconcile regional hydroclimatic records from the EASM region and elucidate their underlying mechanisms.

Acknowledgments: N.S., A.T., S.L., D.C., and K.Y. received funding from the Institute for Basic Science (IBS) under IBS-R028-D1. J.W. acknowledges funding from the Institute for Basic Science under IBS-R028-Y2. K.N.J. would like to thank the Ministry of Education of the Republic of Korea and the National Research Foundation of Korea (NRF-2023R1A2C1006352) for partial funding support. The simulations were conducted on the IBS/ICCP supercomputer "Aleph," a 1.43 petaflops high-performance Cray XC50-LC Skylake computing system with 18,720 processor cores, 9.59 PB of storage, and 43 PB of tap archive space. We also acknowledge the support of KREONET. We thank Jiang Zhu, Jesse Nusbaumer, Robert Tomas, and Jun Hu for their assistance in resolving issues with the iCESM1.2 installation/simulations on Aleph. Dr. Ryoma Hayashi from the Lake Biwa Museum, Japan, is acknowledged for providing lake data and engaging in insightful discussions. The authors gratefully acknowledge discussions with Dr. Ji-Eun Kim from the IBS Center for Climate Physics regarding precessional rainfall variability over China.

Author contributions: N.S. and A.T. conceived the study. K.N.J. provided the Korean speleothem $\delta^{18}O$ records. N.S. performed the model simulations with S.-S.L. and K.-S.Y. on Aleph. N.S. analyzed model data with inputs from A.T. and S.-S.L. N.S. prepared all figures, interpreted the results with A.T., S.-S.L., and J.A.W., and wrote the first draft. Inputs from A.T., D.M.C., J.A.W., and S.-S.L. improved the overall structure of the manuscript. All authors reviewed the final manuscript.

Data Availability:

The Korean speleothem $\delta^{18}O$ record is included in the supplementary material (Table S3).

Competing interests:

The author(s) declare no competing interests.

References

Araguás-Araguás, L., Froehlich, K., and Rozanski, K.: Stable isotope composition of precipitation over southeast Asia, J. Geophys. Res., 103, 28721–28742, https://doi.org/10.1029/98JD02582, 1998.

Araguás-Araguás, L., Froehlich, K., and Rozanski, K.: Deuterium and oxygen-18 isotope composition of precipitation and atmospheric moisture, Hydrol. Process., 14, 1341–1355, https://doi.org/10.1002/1099-1085(20000615)14:8%3C1341::AID-HYP983%3E3.0.CO;2-Z, 2000.

Battisti, D. S., Ding, Q., and Roe, G. H.: Coherent pan-Asian climatic and isotopic response to orbital forcing of tropical insolation, J. Geophys. Res. Atmos., 119, 11,997-12,020, https://doi.org/10.1002/2014JD021960, 2014.

Beck, J. W., Zhou, W., Li, C., Wu, Z., White, L., Xian, F., Kong, X., and An, Z.: A 550,000-year record of East Asian monsoon rainfall from ^{10}Be in loess, Science, 360, 877–881, https://doi.org/10.1126/science.aam5825, 2018.

Berger, A. and Loutre, M. F.: Insolation values for the climate of the last 10 million years, Quaternary Science Reviews, 10, 297–317, https://doi.org/10.1016/0277-3791(91)90033-Q, 1991.

Bosmans, J. H. C., Erb, M. P., Dolan, A. M., Drijfhout, S. S., Tuenter, E., Hilgen, F. J., Edge, D., Pope, J. O., and Lourens, L. J.: Response of the Asian summer monsoons to idealized precession and obliquity forcing in a set of GCMs, Quaternary Science Reviews, 188, 121–135, https://doi.org/10.1016/j.quascirev.2018.03.025, 2018.

Brady, E., Stevenson, S., Bailey, D., Liu, Z., Noone, D., Nusbaumer, J., Otto-Bliesner, B. L., Tabor, C., Tomas, R., Wong, T., Zhang, J., and Zhu, J.: The Connected Isotopic Water Cycle in the Community Earth System Model Version 1, J Adv Model Earth Syst, 11, 2547–2566, https://doi.org/10.1029/2019MS001663, 2019.

Braun, K., Nehme, C., Pickering, R., Rogerson, M., and Scroxton, N.: A Window into Africa's Past Hydroclimates: The SISAL_v1 Database Contribution, Quaternary, 2, 4, https://doi.org/10.3390/quat2010004, 2019.

Cai, Y., Fung, I. Y., Edwards, R. L., An, Z., Cheng, H., Lee, J.-E., Tan, L., Shen, C.-C., Wang, X., Day, J. A., Zhou, W., Kelly, M. J., and Chiang, J. C. H.: Variability of stalagmite-inferred Indian monsoon precipitation over the past 252,000 y, Proc. Natl. Acad. Sci. U.S.A., 112, 2954–2959, https://doi.org/10.1073/pnas.1424035112, 2015.

Chen, T.-J. G. and Chang, C.-P.: The Structure and Vorticity Budget of an Early Summer Monsoon Trough (Mei-Yu) over Southeastern China and Japan, Mon. Wea. Rev., 108, 942–953, https://doi.org/10.1175/1520-0493(1980)108%3C0942:TSAVBO%3E2.0.CO;2, 1980.

Cheng, H., Edwards, R. L., Broecker, W. S., Denton, G. H., Kong, X., Wang, Y., Zhang, R., and Wang, X.: Ice Age Terminations, Science, 326, 248–252, https://doi.org/10.1126/science.1177840, 2009.

Cheng, H., Edwards, R. L., Sinha, A., Spötl, C., Yi, L., Chen, S., Kelly, M., Kathayat, G., Wang, X., Li, X., Kong, X., Wang, Y., Ning, Y., and Zhang, H.: The Asian monsoon over the past 640,000 years and ice age terminations, Nature, 534, 640–646, https://doi.org/10.1038/nature18591, 2016.

Cheng, H., Zhang, H., Zhao, J., Li, H., Ning, Y., and Kathayat, G.: Chinese stalagmite paleoclimate researches: A review and perspective, Sci. China Earth Sci., 62, 1489–1513, https://doi.org/10.1007/s11430-019-9478-3, 2019.

Cheng, H., Zhang, H., Cai, Y., Shi, Z., Yi, L., Deng, C., Hao, Q., Peng, Y., Sinha, A., Li, H., Zhao, J., Tian, Y., Baker, J., and Perez-Mejías, C.: Orbital-scale Asian summer monsoon variations: Paradox and exploration, Sci. China Earth Sci., 64, 529–544, https://doi.org/10.1007/s11430-020-9720-y, 2021.

Chiang, J. C. H., Fung, I. Y., Wu, C.-H., Cai, Y., Edman, J. P., Liu, Y., Day, J. A., Bhattacharya, T., Mondal, Y., and Labrousse, C. A.: Role of seasonal transitions and westerly jets in East Asian paleoclimate, Quaternary Science Reviews, 108, 111–129, https://doi.org/10.1016/j.quascirev.2014.11.009, 2015.

Chiang, J. C. H., Swenson, L. M., and Kong, W.: Role of seasonal transitions and the westerlies in the interannual variability of the East Asian summer monsoon precipitation, Geophys. Res. Lett., 44, 3788–3795, https://doi.org/10.1002/2017GL072739, 2017.

Chu, J.-E., Lee, S.-S., Timmermann, A., Wengel, C., Stuecker, M. F., and Yamaguchi, R.: Reduced tropical cyclone densities and ocean effects due to anthropogenic greenhouse warming, Sci. Adv., 6, eabd5109, https://doi.org/10.1126/sciadv.abd5109, 2020.

Clemens, S. C., Holbourn, A., Kubota, Y., Lee, K. E., Liu, Z., Chen, G., Nelson, A., and Fox-Kemper, B.: Precession-band variance missing from East Asian monsoon runoff, Nat Commun, 9, 3364, https://doi.org/10.1038/s41467-018-05814-0, 2018.

Clement, A. C., Hall, A., and Broccoli, A. J.: The importance of precessional signals in the tropical climate, Climate Dynamics, 22, 327–341, https://doi.org/10.1007/s00382-003-0375-8, 2004.

Craig, H. and Gordon, L. I.: Deuterium and oxygen 18 variations in the ocean and marine atmosphere, 1965.

Dai, G., Zhang, Z., Otterå, O. H., Langebroek, P. M., Yan, Q., and Zhang, R.: A Modeling Study of the Tripole Pattern of East China Precipitation Over the Past 425 ka, JGR Atmospheres, 126, e2020JD033513, https://doi.org/10.1029/2020JD033513, 2021.

Dansgaard, W.: Stable isotopes in precipitation, Tellus, 16, 436–468, https://doi.org/10.1111/j.2153-3490.1964.tb00181.x, 1964.

Ding, Y.: Seasonal March of The East-Asian Summer Monsoon, in: World Scientific Series on Asia-Pacific Weather and Climate, vol. 02, World Scientific, 3–53, https://doi.org/10.1142/9789812701411_0001, 2004.

Fairchild, I. J., Smith, C. L., Baker, A., Fuller, L., Spötl, C., Mattey, D., McDermott, F., and E.I.M.F.: Modification and preservation of environmental signals in speleothems, Earth-Science Reviews, 75, 105–153, https://doi.org/10.1016/j.earscirev.2005.08.003, 2006.

Gasse, F., Vidal, L., Develle, A.-L., and Van Campo, E.: Hydrological variability in the Northern Levant: a 250 ka multi-proxy record from the Yammoûneh (Lebanon) sedimentary sequence, Clim. Past, 7, 1261–1284, https://doi.org/10.5194/cp-7-1261-2011, 2011.

Gat, J. R.: Oxygen and hydrogen isotopes in the hydrologic cycle, Annu. Rev. Earth Planet. Sci., 24, 225–262, https://doi.org/10.1146/annurev.earth.24.1.225, 1996.

Gat, J. R., Bowser, C. J., and Kendall, C.: The contribution of evaporation from the Great Lakes to the continental atmosphere: estimate based on stable isotope data, Geophysical Research Letters, 21, 557–560, https://doi.org/10.1029/94GL00069, 1994.

Ha, K., Heo, K., Lee, S., Yun, K., and Jhun, J.: Variability in the East Asian Monsoon: a review, Meteorological Applications, 19, 200–215, https://doi.org/10.1002/met.1320, 2012.

Hayashi, R., Takahara, H., Inouchi, Y., Takemura, K., and Igarashi, Y.: Vegetation and endemic tree response to orbital-scale climate changes in the Japanese archipelago during the last glacial–interglacial cycle based on pollen records from Lake Biwa, western Japan, Review of Palaeobotany and Palynology, 241, 85–97, https://doi.org/10.1016/j.revpalbo.2017.02.008, 2017.

Hayashi, R., Sagawa, T., Irino, T., and Tada, R.: Orbital-scale vegetation-ocean-atmosphere linkages in western Japan during the last 550 ka based on a pollen record from the IODP site U1427 in the Japan Sea, Quaternary Science Reviews, 267, 107103, https://doi.org/10.1016/j.quascirev.2021.107103, 2021.

He, C., Liu, Z., Otto-Bliesner, B. L., Brady, E. C., Zhu, C., Tomas, R., Clark, P. U., Zhu, J., Jahn, A., Gu, S., Zhang, J., Nusbaumer, J., Noone, D., Cheng, H., Wang, Y., Yan, M., and Bao, Y.: Hydroclimate footprint of pan-Asian monsoon water isotope during the last deglaciation, Sci. Adv., 7, eabe2611, https://doi.org/10.1126/sciadv.abe2611, 2021.

Held, F., Cheng, H., Edwards, R. L., Kipfer, T., Tüysüz, O., Koç, K., Affolter, S., and Fleitmann, D.: Hydrological variability in the Black Sea region during the last 670,000 years recorded in multi-proxy speleothem records from northern Türkiye, Quaternary Science Reviews, 367, 109534, https://doi.org/10.1016/j.quascirev.2025.109534, 2025.

Hu, J., Emile-Geay, J., Tabor, C., Nusbaumer, J., and Partin, J.: Deciphering Oxygen Isotope Records From Chinese Speleothems With an Isotope-Enabled Climate Model, Paleoceanography and Paleoclimatology, 34, 2098–2112, https://doi.org/10.1029/2019PA003741, 2019.

Huang, L., Lee, S., and Timmermann, A.: Caspian Sea and Black Sea Response to Greenhouse Warming in a High-Resolution Global Climate Model, Geophys Res Lett, 48, https://doi.org/10.1029/2020GL090270, 2021.

Igarashi, Y. and Oba, T.: Fluctuations in the East Asian monsoon over the last 144ka in the northwest Pacific based on a high-resolution pollen analysis of IMAGES core MD01-2421, Quaternary Science Reviews, 25, 1447–1459, https://doi.org/10.1016/j.quascirev.2005.11.011, 2006.

Iwamoto, N. and Inouchi, Y.: Reconstruction of millennial-scale variations in the East Asian summer monsoon over the past 300 ka based on the total carbon content of sediment from Lake Biwa, Japan, Environ Geol, 52, 1607–1616, https://doi.org/10.1007/s00254-006-0606-5, 2007.

Jo, K., Woo, K. S., Cheng, H., Edwards, L. R., Wang, Y., Kim, R., and Jiang, X.: Textural and carbon isotopic evidence of monsoonal changes recorded in a composite-type speleothem from Korea since MIS 5a, Quat. res., 74, 100–112, https://doi.org/10.1016/j.yqres.2010.04.005, 2010.

Jo, K., Woo, K. S., Lim, H. S., Cheng, H., Edwards, R. L., Wang, Y., Jiang, X., Kim, R., Lee, J. I., Yoon, H. I., and Yoo, K.-C.: Holocene and Eemian climatic optima in the Korean Peninsula based on textural and carbon isotopic records from the stalagmite of the Daeya Cave, South Korea, Quaternary Science Reviews, 30, 1218–1231, https://doi.org/10.1016/j.quascirev.2011.02.012, 2011.

Jo, K., Woo, K. S., Yi, S., Yang, D. Y., Lim, H. S., Wang, Y., Cheng, H., and Edwards, R. L.: Mid-latitude interhemispheric hydrologic seesaw over the past 550,000 years, Nature, 508, 378–382, https://doi.org/10.1038/nature13076, 2014.

Jo, K., Yi, S., Lee, J.-Y., Woo, K. S., Cheng, H., Edwards, L. R., and Kim, S.-T.: 1000-Year Quasi-Periodicity of Weak Monsoon Events in Temperate Northeast Asia since the Mid-Holocene, Scientific Reports, 7, 15196, https://doi.org/10.1038/s41598-017-15566-4, 2017.

Jo, K. N., Woo, K. S., Kim, J. C., Yang, D. Y., Lawrence, E. R., Cheng, H., and Wang, Y.: Paleoclimatic implications recorded in the late Pleistocene stalagmite, Eden Cave, Danyang, Korea, jgsk, 42, 127–142, https://doi.org/10.14770/jgsk.2006.42.1.127, 2006.

Jouzel, J., Delaygue, G., Landais, A., Masson-Delmotte, V., Risi, C., and Vimeux, F.: Water isotopes as tools to document oceanic sources of precipitation: Water Isotopes and Precipitation Origin, Water Resour. Res., 49, 7469–7486, https://doi.org/10.1002/2013WR013508, 2013.

Jung, Y.-Y., Shin, W.-J., Seo, K.-H., Koh, D.-C., Ko, K.-S., and Lee, K.-S.: Spatial distributions of oxygen and hydrogen isotopes in multi-level groundwater across South Korea: A case study of mountainous regions, Science of The Total Environment, 812, 151428, https://doi.org/10.1016/j.scitotenv.2021.151428, 2022.

Kathayat, G., Cheng, H., Sinha, A., Spötl, C., Edwards, R. L., Zhang, H., Li, X., Yi, L., Ning, Y., Cai, Y., Lui, W. L., and Breitenbach, S. F. M.: Indian monsoon variability on millennial-orbital timescales, Sci Rep, 6, 24374, https://doi.org/10.1038/srep24374, 2016.

Kato, H., Amekawa, S., Hori, M., Shen, C.-C., Kuwahara, Y., Senda, R., and Kano, A.: "Influences of temperature and the meteoric water δ18O value on a stalagmite record in the last deglacial to middle Holocene period from southwestern Japan," Quaternary Science Reviews, 253, 106746, https://doi.org/10.1016/j.quascirev.2020.106746, 2021.

Kim, S., Han, Y., Hur, S. D., Yoshimura, K., and Lee, J.: Relating Moisture Transport to Stable Water Vapor Isotopic Variations of Ambient Wintertime along the Western Coast of Korea, Atmosphere, 10, 806, https://doi.org/10.3390/atmos10120806, 2019.

Kutzbach, J. E., Liu, X., Liu, Z., and Chen, G.: Simulation of the evolutionary response of global summer monsoons to orbital forcing over the past 280,000 years, Clim Dyn, 30, 567–579, https://doi.org/10.1007/s00382-007-0308-z, 2008.

Lachniet, M. S.: Climatic and environmental controls on speleothem oxygen-isotope values, Quaternary Science Reviews, 28, 412–432, https://doi.org/10.1016/j.quascirev.2008.10.021, 2009.

Lee, J., Fox-Kemper, B., Horvat, C., and Ming, Y.: The Response of East Asian Monsoon to the Precessional Cycle: A New Study Using the Geophysical Fluid Dynamics Laboratory Model, Geophysical Research Letters, 46, 11388–11396, https://doi.org/10.1029/2019GL082661, 2019.

Lee, K.S., Woo, N.C., and Kim, K.: Factors controlling stable isotope composition of precipitation in Northeast Asia, JGSK, 37, 183–192, 2001.

Li, X., Zhou, Y., Han, Z., Yuan, X., Yi, S., Zeng, Y., Qin, L., Lu, M., and Lu, H.: Loess deposits in the low latitudes of East Asia reveal the ~20-kyr precipitation cycle, Nat Commun, 15, 1023, https://doi.org/10.1038/s41467-024-45379-9, 2024.

Lin, F., Zhang, Q., Sinha, A., Wang, Z., Axelsson, J., Chen, L., Wang, T., and Tan, L.: Seasonal to decadal variations of precipitation oxygen isotopes in northern China linked to the moisture source, npj Clim Atmos Sci, 7, 14, https://doi.org/10.1038/s41612-024-00564-x, 2024.

Liu, X., Xie, X., Guo, Z., Yin, Z.-Y., and Chen, G.: Model-based orbital-scale precipitation δ18O variations and distinct mechanisms in Asian monsoon and arid regions, National Science Review, 9, nwac182, https://doi.org/10.1093/nsr/nwac182, 2022.

Liu, Z., Wen, X., Brady, E. C., Otto-Bliesner, B., Yu, G., Lu, H., Cheng, H., Wang, Y., Zheng, W., Ding, Y., Edwards, R. L., Cheng, J., Liu, W., and Yang, H.: Chinese cave records and the East Asia Summer Monsoon, Quaternary Science Reviews, 83, 115–128, https://doi.org/10.1016/j.quascirev.2013.10.021, 2014.

Lorenz, S. J. and Lohmann, G.: Acceleration technique for Milankovitch type forcing in a coupled atmosphere-ocean circulation model: method and application for the Holocene, Climate Dynamics, 23, 727–743, https://doi.org/10.1007/s00382-004-0469-y, 2004a.

Lorenz, S. J. and Lohmann, G.: Acceleration technique for Milankovitch type forcing in a coupled atmosphere-ocean circulation model: method and application for the Holocene, Climate Dynamics, 23, 727–743, https://doi.org/10.1007/s00382-004-0469-y, 2004b.

Maher, B. A. and Thompson, R.: Oxygen isotopes from Chinese caves: records not of monsoon rainfall but of circulation regime, J Quaternary Science, 27, 615–624, https://doi.org/10.1002/jqs.2553, 2012.

Masson-Delmotte, V., Jouzel, J., Landais, A., Stievenard, M., Johnsen, S. J., White, J. W. C., Werner, M., Sveinbjornsdottir, A., and Fuhrer, K.: GRIP Deuterium Excess Reveals Rapid and Orbital-Scale Changes in Greenland Moisture Origin, Science, 309, 118–121, https://doi.org/10.1126/science.1108575, 2005.

Matthews, A., Affek, H. P., Ayalon, A., Vonhof, H. B., and Bar-Matthews, M.: Eastern Mediterranean climate change deduced from the Soreq Cave fluid inclusion stable isotopes and carbonate clumped isotopes record of the last 160 ka, Quaternary Science Reviews, 272, 107223, https://doi.org/10.1016/j.quascirev.2021.107223, 2021.

Merlivat, L. and Jouzel, J.: Global climatic interpretation of the deuterium-oxygen 18 relationship for precipitation, J. Geophys. Res., 84, 5029, https://doi.org/10.1029/JC084iC08p05029, 1979.

Mori, T., Kashiwagi, K., Amekawa, S., Kato, H., Okumura, T., Takashima, C., Wu, C.-C., Shen, C.-C., Quade, J., and Kano, A.: Temperature and seawater isotopic controls on two stalagmite records since 83 ka from maritime Japan, Quaternary Science Reviews, 192, 47–58, https://doi.org/10.1016/j.quascirev.2018.05.024, 2018.

Park, Y., Lee, K.S., and Yu, J.Y.: Seasonal variations of dissolved ions and oxygen and hydrogen isotopic compositions of precipitation in Chuncheon, Korea, JGSK, 42, 283–292, 2006.

Pausata, F. S. R., Battisti, D. S., Nisancioglu, K. H., and Bitz, C. M.: Chinese stalagmite δ18O controlled by changes in the Indian monsoon during a simulated Heinrich event, Nature Geosci, 4, 474–480, https://doi.org/10.1038/ngeo1169, 2011.

Pfahl, S. and Sodemann, H.: What controls deuterium excess in global precipitation?, Clim. Past, 10, 771–781, https://doi.org/10.5194/cp-10-771-2014, 2014.

Raavi, P. H., Chu, J.-E., Timmermann, A., Lee, S.-S., and Walsh, K. J. E.: Moisture control of tropical cyclones in high-resolution simulations of paleoclimate and future climate, Nat Commun, 14, 6426, https://doi.org/10.1038/s41467-023-42033-8, 2023.

Risi, C., Bony, S., and Vimeux, F.: Influence of convective processes on the isotopic composition (δ^{18} O and δ D) of precipitation and water vapor in the tropics: 2. Physical interpretation of the amount effect, J. Geophys. Res., 113, 2008JD009943, https://doi.org/10.1029/2008JD009943, 2008.

Sha, L., Mahata, S., Duan, P., Luz, B., Zhang, P., Baker, J., Zong, B., Ning, Y., Brahim, Y. A., Zhang, H., Edwards, R. L., and Cheng, H.: A novel application of triple oxygen isotope ratios of speleothems, Geochimica et Cosmochimica Acta, 270, 360–378, https://doi.org/10.1016/j.gca.2019.12.003, 2020.

Sha, L., Wassenburg, J. A., Sha, L., Li, Y., Zhou, S., Liang, Q., Zhao, J., Ruan, J., Li, H., Zhao, X., Duan, P., Wang, J., Lu, J., Zhang, H., Kathayat, G., Mahata, S., Ban, F., Li, T.-Y., and Cheng, H.: Variations in triple oxygen isotope of speleothems from the Asian monsoon region reveal moisture sources over the past 300 years, Commun Earth Environ, 4, 384, https://doi.org/10.1038/s43247-023-01043-6, 2023.

Sinha, N., Chakraborty, S., and Mohan, P. M.: Modern rain-isotope data from Indian island and the mainland on the daily scale for the summer monsoon season, Data in Brief, 23, 103793, https://doi.org/10.1016/j.dib.2019.103793, 2019.

Stewart, M. K.: Stable isotope fractionation due to evaporation and isotopic exchange of falling waterdrops: Applications to atmospheric processes and evaporation of lakes, J. Geophys. Res., 80, 1133–1146, https://doi.org/10.1029/JC080i009p01133, 1975.

Sun, J. and Huang, X.: Half-precessional cycles recorded in Chinese loess: response to low-latitude insolation forcing during the Last Interglaciation, Quaternary Science Reviews, 25, 1065–1072, https://doi.org/10.1016/j.quascirev.2005.08.004, 2006.

Sun, Y., Clemens, S. C., An, Z., and Yu, Z.: Astronomical timescale and palaeoclimatic implication of stacked 3.6-Myr monsoon records from the Chinese Loess Plateau, Quaternary Science Reviews, 25, 33–48, https://doi.org/10.1016/j.quascirev.2005.07.005, 2006.

Tabor, C. R., Otto-Bliesner, B. L., Brady, E. C., Nusbaumer, J., Zhu, J., Erb, M. P., Wong, T. E., Liu, Z., and Noone, D.: Interpreting Precession-Driven $\delta^{18}O$ Variability in the South Asian Monsoon Region, J. Geophys. Res. Atmos., 123, 5927–5946, https://doi.org/10.1029/2018JD028424, 2018.

Tarasov, P. E., Nakagawa, T., Demske, D., Österle, H., Igarashi, Y., Kitagawa, J., Mokhova, L., Bazarova, V., Okuda, M., Gotanda, K., Miyoshi, N., Fujiki, T., Takemura, K., Yonenobu, H., and Fleck, A.: Progress in the reconstruction of Quaternary climate dynamics in the Northwest Pacific: A new modern analogue reference dataset and its application to the 430-kyr pollen record from Lake Biwa, Earth-Science Reviews, 108, 64–79, https://doi.org/10.1016/j.earscirev.2011.06.002, 2011.

Timmermann, A., Lorenz, S. J., An, S.-I., Clement, A., and Xie, S.-P.: The Effect of Orbital Forcing on the Mean Climate and Variability of the Tropical Pacific, Journal of Climate, 20, 4147–4159, https://doi.org/10.1175/JCLI4240.1, 2007.

Timmermann, A., Yun, K.-S., Raia, P., Ruan, J., Mondanaro, A., Zeller, E., Zollikofer, C., Ponce de León, M., Lemmon, D., Willeit, M., and Ganopolski, A.: Climate effects on archaic human habitats and species successions, Nature, 604, 495–501, https://doi.org/10.1038/s41586-022-04600-9, 2022.

Uemura, R., Matsui, Y., Yoshimura, K., Motoyama, H., and Yoshida, N.: Evidence of deuterium excess in water vapor as an indicator of ocean surface conditions, J. Geophys. Res., 113, D19114, https://doi.org/10.1029/2008JD010209, 2008.

Volonté, A., Turner, A. G., Schiemann, R., Vidale, P. L., and Klingaman, N. P.: Characterising the interaction of tropical and extratropical air masses controlling East Asian summer monsoon progression using a novel frontal detection approach, Weather Clim. Dynam., 3, 575–599, https://doi.org/10.5194/wcd-3-575-2022, 2022.

Wang, B. and Lin: Rainy Season of the Asian–Pacific Summer Monsoon, J. Climate, 15, 386–398, https://doi.org/10.1175/1520-0442(2002)015%3C0386:RSOTAP%3E2.0.CO;2, 2002.

Wang, B., Wu, Z., Li, J., Liu, J., Chang, C.-P., Ding, Y., and Wu, G.: How to Measure the Strength of the East Asian Summer Monsoon, Journal of Climate, 21, 4449–4463, https://doi.org/10.1175/2008JCLI2183.1, 2008.

Wang, Y. J., Cheng, H., Edwards, R. L., An, Z. S., Wu, J. Y., Shen, C.-C., and Dorale, J. A.: A High-Resolution Absolute-Dated Late Pleistocene Monsoon Record from Hulu Cave, China, Science, 294, 2345–2348, https://doi.org/10.1126/science.1064618, 2001.

Wen, Q., Liu, Z., Jing, Z., Clemens, S. C., Wang, Y., Yan, M., Ning, L., and Liu, J.: Grand dipole response of Asian summer monsoon to orbital forcing, npj Clim Atmos Sci, 7, 202, https://doi.org/10.1038/s41612-024-00749-4, 2024.

Wengel, C., Lee, S.-S., Stuecker, M. F., Timmermann, A., Chu, J.-E., and Schloesser, F.: Future high-resolution El Niño/Southern Oscillation dynamics, Nature Climate Change, 11, 758–765, https://doi.org/10.1038/s41558-021-01132-4, 2021.

Wu, C.-H., Lee, S.-Y., and Chiang, J. C. H.: Relative influence of precession and obliquity in the early Holocene: Topographic modulation of subtropical seasonality during the Asian summer monsoon, Quaternary Science Reviews, 191, 238–255, https://doi.org/10.1016/j.quascirev.2018.05.021, 2018.

Xia, Z., Surma, J., and Winnick, M. J.: The response and sensitivity of deuterium and 17O excess parameters in precipitation to hydroclimate processes, Earth-Science Reviews, 242, 104432, https://doi.org/10.1016/j.earscirev.2023.104432, 2023.

Xie, X., Liu, X., Chen, G., and Korty, R. L.: A Transient Modeling Study of the Latitude Dependence of East Asian Winter Monsoon Variations on Orbital Timescales, Geophysical Research Letters, 46, 7565–7573, https://doi.org/10.1029/2019GL083060, 2019.

Xue, G., Cai, Y., Zheng, Y., Zhang, H., Han, T., Huang, S., Cheng, X., Ma, L., Liu, C., Edwards, R. L., Cheng, H., and Yan, H.: Western Pacific Subtropical High Modulates Regional Hydroclimate Changes on Multiple Timescales Over Central China, JGR Atmospheres, 130, e2024JD042735, https://doi.org/10.1029/2024JD042735, 2025.

Yang, H., Chou, Y.-M., Jiang, X., Zheng, W., He, Y., Banerjee, Y., Shen, C.-C., Yu, T.-L., Zhong, Y., Humbert, F., and Liu, Q.: Chinese stalagmite $\delta^{18}O$ records reveal the diverse moisture trajectories during the middle to late last glacial period, Geol. Mag., 1–13, https://doi.org/10.1017/S0016756824000013, 2024.

Yoshimura, K. and Ichiyanagi, K.: A reconsideration of Seasonal Variation in Precipitation Deuterium Excess Over East Asia, J. Japan Soc. Hydrol. and Water Resour., 22, 262–276, https://doi.org/10.3178/jjshwr.22.262, 2009.

Yoshimura, K., Kanamitsu, M., Noone, D., and Oki, T.: Historical isotope simulation using Reanalysis atmospheric data, J. Geophys. Res., 113, D19108, https://doi.org/10.1029/2008JD010074, 2008.

Yun, K.-S., Timmermann, A., Lee, S.-S., Willeit, M., Ganopolski, A., and Jadhav, J.: A transient coupled general circulation model (CGCM) simulation of the past 3 million years, Clim. Past, 19, 1951–1974, https://doi.org/10.5194/cp-19-1951-2023, 2023.

Zeller, E., Timmermann, A., Yun, K.-S., Raia, P., Stein, K., and Ruan, J.: Human adaptation to diverse biomes over the past 3 million years, Science, 380, 604–608, https://doi.org/10.1126/science.abq1288, 2023.

Zhang, H., Griffiths, M. L., Chiang, J. C. H., Kong, W., Wu, S., Atwood, A., Huang, J., Cheng, H., Ning, Y., and Xie, S.: East Asian hydroclimate modulated by the position of the westerlies during Termination I, Science, 362, 580–583, https://doi.org/10.1126/science.aat9393, 2018.

Zhao, L., Xiao, H., Zhou, M., Cheng, G., Wang, L., Yin, L., and Ren, J.: Factors controlling spatial and seasonal distributions of precipitation δ^{18}O in China, Hydrological Processes, 26, 143–152, https://doi.org/10.1002/hyp.8118, 2012.

Zheng, Y., Liu, H., Yang, H., Wang, H., Zhao, W., Zhang, Z., Huang, M., and Liu, W.: Decoupled Asian monsoon intensity and precipitation during glacial-interglacial transitions on the Chinese Loess Plateau, Nat Commun, 13, 5397, https://doi.org/10.1038/s41467-022-33105-2, 2022.

Zhu, H., Zhu, L., Luo, L., and Li, J.: Seasonal Variations of Modern Precipitation Stable Isotopes over the North Tibetan Plateau and Their Influencing Factors, Water, 16, 150, https://doi.org/10.3390/w16010150, 2023.

Muted orbital-scale Monsoon Variability over the Korean Peninsula

Nitesh Sinha[1,2], Axel Timmermann[1,2], Sun-Seon Lee[1,2], Kyoung-Nam Jo[3], Jasper A. Wassenburg[1,2], Daniel M. Cleary[1,2], Kyung-Sook Yun[1,2]

[1]Center for Climate Physics, Institute for Basic Science, Busan, Republic of Korea
[2]Pusan National University, Busan, Republic of Korea
[3]Kangwon National University, Chuncheon, Gangwon-do, Republic of Korea

Correspondence to: nitesh@pusan.ac.kr

This file includes:

Figures S1 to S16
Section S1-S2
Tables S1 to S3
SI References

Deleted: 5

Deleted: Table S2

Section S1: Tagging Experiment

The water tagging experiment has been conducted with the iCESM, and we used the following source regions (Figure S7):

Deleted: 7

Land Tagging:

SAS - South Asia, **CAS** - Central Asia, **TAS** - Tropical Asia, **EAS** - East Asia, **NAS** - North Asia, **AFR** – Africa, **EUR** – Europe, **LND** – All land.

Ocean Tagging:

NNP - northern North Pacific, **SNP** - subtropical North Pacific, **EEP** - east equatorial Pacific, **WEP** - west equatorial Pacific, **SSP** - subtropical South Pacific, **EQI** - equatorial Indian, **SSI** - subtropical South Indian.

P is the total precipitation at the target location (KP) with contributions P_i from all the tagged source regions.

$$P = \sum_{i=1}^{n} P_i$$

$\delta^{18}O_p$ at a particular grid cell is the sum of precipitation-$\delta^{18}O_i$ originating from all tagged source regions (i), weighted by their precipitation contribution:

$$\delta^{18}O_p = \sum_{i=1}^{n} \delta^{18}O_i \frac{P_i}{P}$$

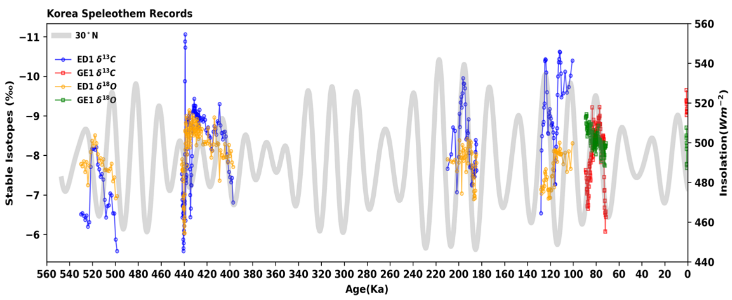

Fig. S1. *Speleothem ($\delta^{13}C$ and $\delta^{18}O$) records from Eden Cave (ED1) and Gwaneum Cave (GE1) in South Korea. Refer to Jo et al.*(Jo et al., 2011, 2014) *for further details.*

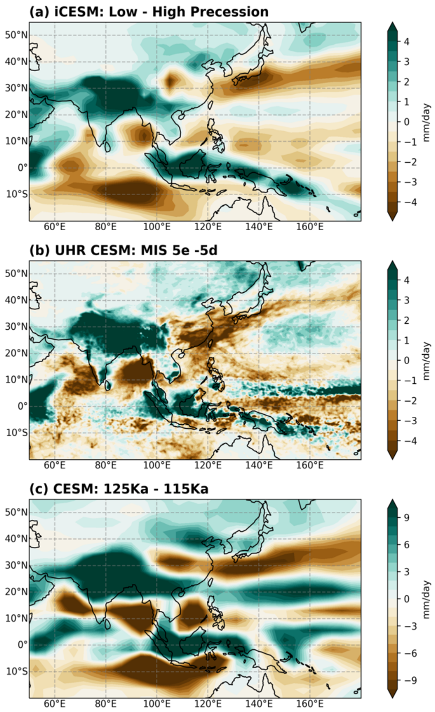

Fig. S2. *Summer mean precipitation differences for (a) Low – High precession from iCESM simulation (~2^o horizontal resolution), (b) MIS5e – MIS5d from ultra-high-resolution (UHR) CESM simulations (~0.25^o horizontal resolution), and (c) time slices for 125 ka – 115 ka from 3Ma transient simulation. (~3.75^o horizontal resolution),*

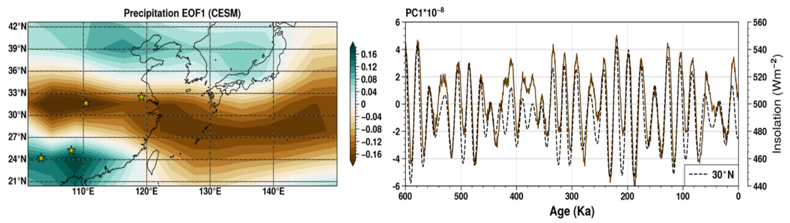

Fig. S3. *First empirical orthogonal function (EOF1) for annual mean precipitation (shaded, left panel) and corresponding principal component (PC1) (brown curve, right panel) for Eastern Asia using 3Ma transient simulation. The EOF analysis is based on the last 600 kyr of the simulation. Major studied caves in China are marked by a yellow star symbol (left panel), refer to Figure 1. The black dashed curve represents summer insolation at 30°N (right panel).*

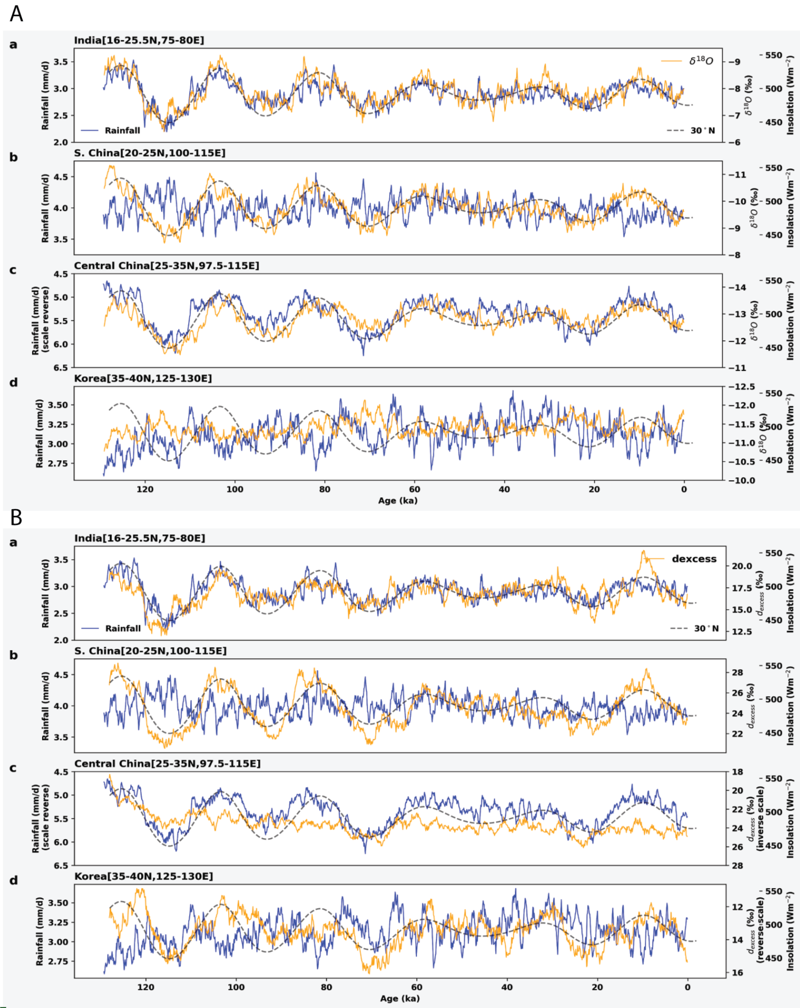

Fig. S4. *Simulated annual mean variations in precipitation (blue curves) for (a) India, (b) South (S.) China, (c) central China, and (d) Korea in the last 130ka from an orbitally forced transient simulation conducted with iCESM1.2. Orange curves in panel A (B) show precipitation-$\delta^{18}O$ (d-excess). Dashed black curves represent insolation (30 °N) insolation changes.*

Moved (insertion) [1]

Deleted: *16*

Section S2

Beck's (Beck et al., 2018) ^{10}Be reconstruction corresponds well to simulated regional rainfall over the Loess area if we shift the ^{10}Be record by ~6 ka (Fig. S5c). The shifted ^{10}Be shows a higher correlation ($R^2 = 0.30$) with the simulated rainfall than the reported $R^2 = 0.16$ with the Sanbao $\delta^{18}O_{sp}$ record. The ^{10}Be record (6 ka shifted) also matches quite well with Cryptomeria pollen records from Japan(Hayashi et al., 2021; Igarashi and Oba, 2006) (Figure 3c). Now, we understand that the precipitation and $\delta^{18}O_p$ spatial patterns as a grand dipole response to orbital forcing(Wen et al., 2024). The age shift may be justified as ^{10}Be age determination uses one of the assumptions that the Chinese speleothem-δ^{18}O record was controlled by regional EASM rainfall intensity. Moreover, our model simulations also do not support the EASM precipitation and $\delta^{18}O_p$ uniform temporal or spatial relationship throughout the region on orbital timescales, such as Chinese speleothem-δ^{18}O does not correspond well with simulated China rainfall but with India rainfall (Fig. S5a and S5b).

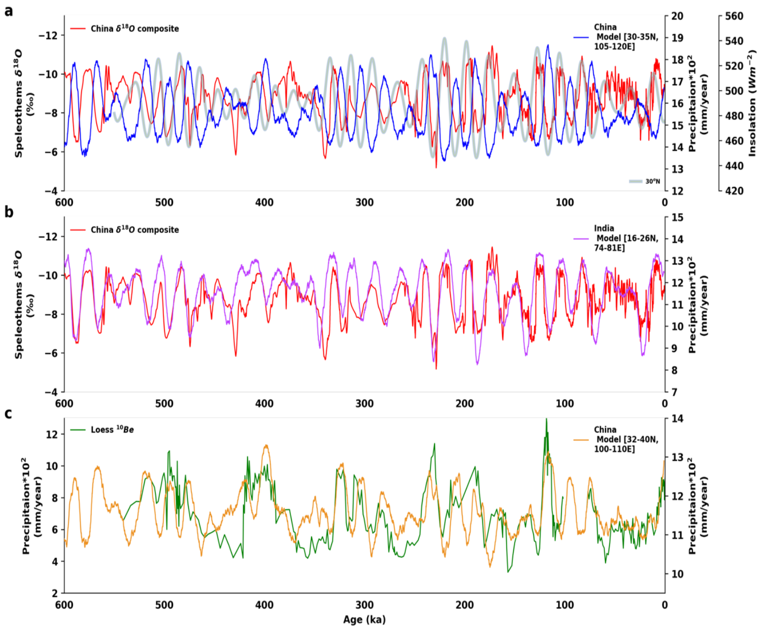

***Fig. S5** Comparison of simulated precipitation change by 3 Ma transient simulation (only the last 600 kyr are shown here) and proxies from (a) Eastern Asia and China speleothem-δ^{18}O composite record, (b) India and China speleothem-δ^{18}O composite record, and (c) China and Loess ^{10}Be record. Summer insolation at 30°N is shown in panel (a).*

Deleted: 4

Deleted: 4

Deleted: 4

Deleted: *4*

Deleted: .

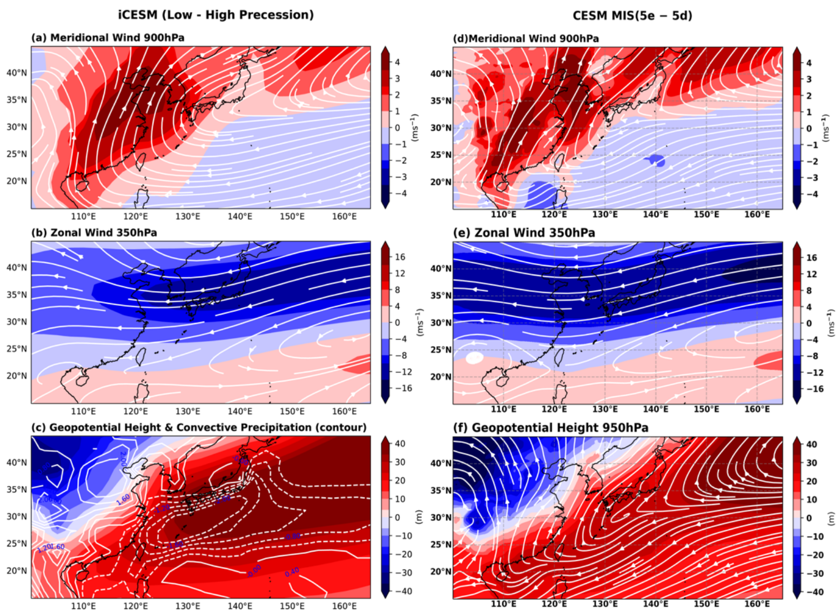

Fig. S6, Differences between Pmin and Pmax in iCESM-130ka (left panels) and between hiresCESM-5d and hiresCESM-5e (right panels). (a)(d) Meridional wind at 900 hPa (shading) and streamlines. (b)(e) Zonal wind at 350 hPa (shading) and streamlines. (c) Geopotential height 950 hPa (shading) and convective precipitation (contour). (f) Geopotential height 950 hPa (shading) and streamlines.

Deleted: ***5***

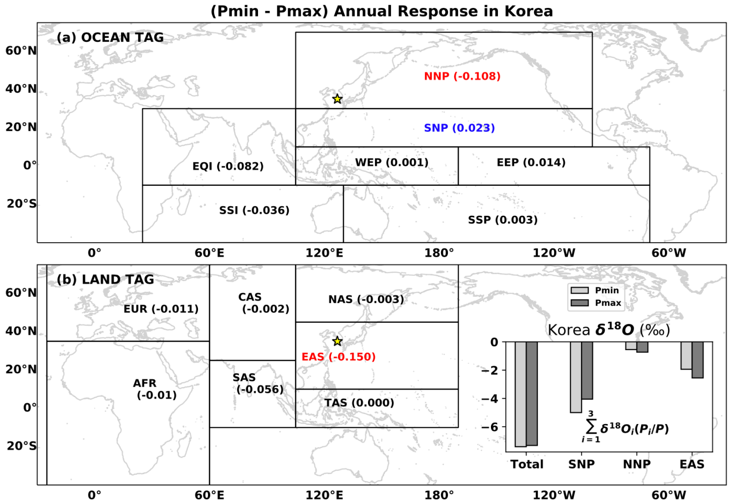

__Figure S7.__ Differences in annual precipitation (mm/day) on the Korean Peninsula between Pmin and Pmax from various moisture sources over (a) ocean and (b) land. Color text is a major contributor to the Korean Peninsula (blue positive and red negative for P_{min} -P_{max}). Inset plot (lower right): the summer precipitation δ18O in Korea from major and near-source contributors from Land (EAS) and the Ocean (SNP, NNP). "Total" represents the precipitation-$\delta^{18}O$ combination from all tag regions in Korea. Korea is marked by a yellow star.

Deleted: ***6***

Deleted: ***:***

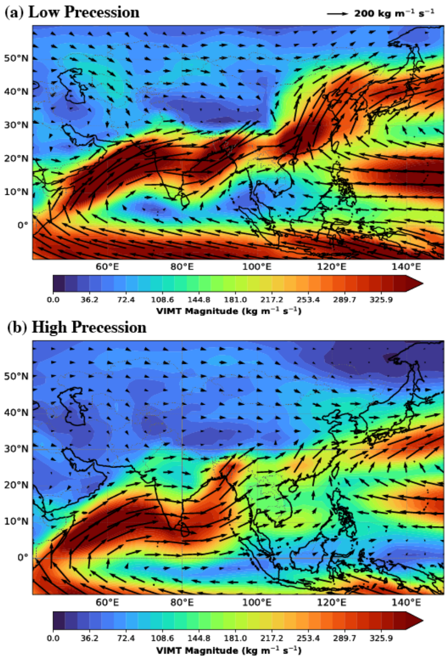

Fig. S8, *Vertically integrated moisture transport (VIMT) during boreal summer (JJA) under low precession (a) and high precession (b) conditions. VIMT magnitude (kg m^{-1} s^{-1}) showing the spatial distribution and intensity of moisture transport across Asia. Black arrows indicate VIMT vector direction and relative magnitude (reference vector: 200 kg m^{-1} s^{-1}).*

Deleted: *7*

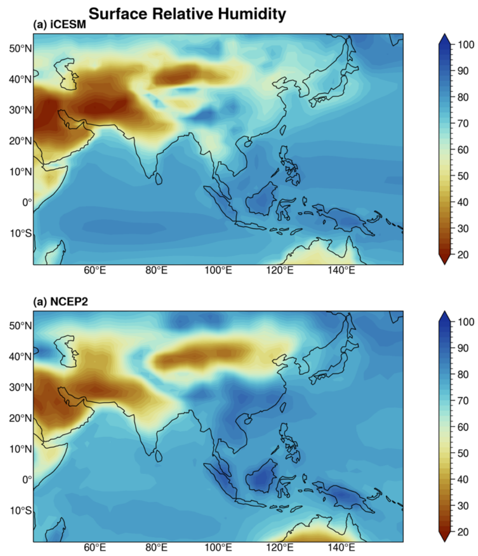

Fig. S9, *(a) Relative humidity simulated in iCESM for present day conditions in comparison to (b) NCEP2 reanalysis data for the last 40 years (accessed through APDRC OPeNDAP Server (http://apdrc.soest.hawaii.edu/index.php). Model captures the spatial pattern reasonably well, except lower humidity over the southeast Asian region.*

Deleted: *8*

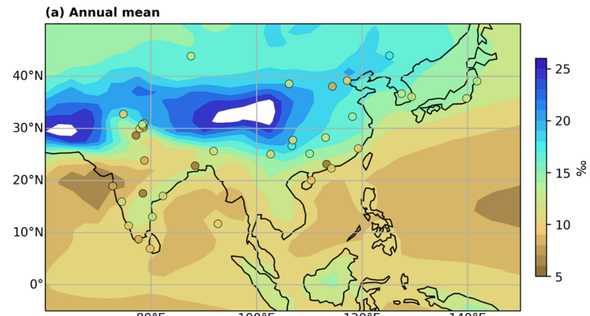

Fig. S10, *Present day iCESM simulated (shaded) d-excess and GNIP sites (circle) annual mean d-excess comparison.*

Deleted: *9*

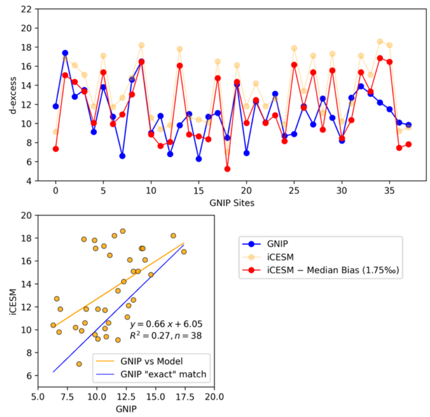

Fig. S11, *Upper panel shows the series of d-excess values for 38 Asian sites, GNIP (blue), iCESM (orange), and iCESM Median bias adjusted (red). Lower left panel shows the correlation between simulated and GNIP mean annual d-excess values for Asian sites. Note: All Asian GNIP sites are considered here, a screening has been applied, such as only the sites which have at least 2 years of data.*

Deleted: *0*

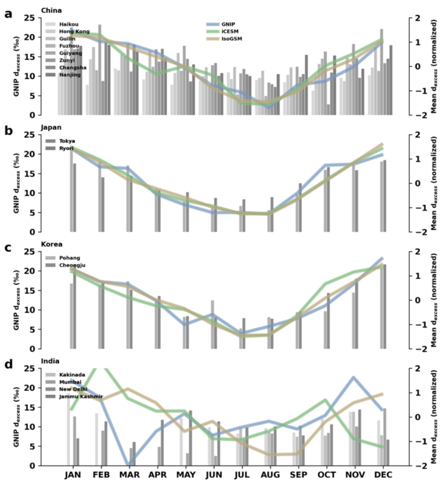

Fig. S12, *A comparison between the monthly climatology of d-excess from GNIP (light blue), iCESM simulation (light green), and IsoGSM2 (light brown) for some of the sites from China, Japan, Korea, and India. Gray bars show mean monthly d-excess for individual GNIP sites, gray shading represents site latitude from low to high (lighter to darker).*

Deleted: *1*

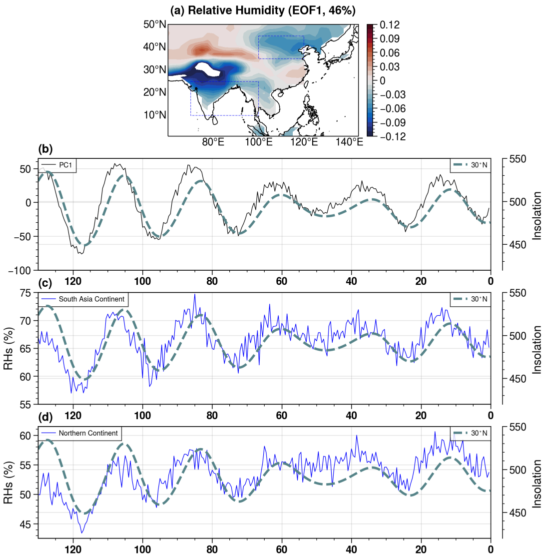

Fig. S13, *First empirical orthogonal function (EOF1(a)) and corresponding principal component (PC1, b) for the summer mean surface relative humidity for the 130 ka transient simulation on iCESM1.2. Temporal evolution of surface relative humidity over continental regions (c, d). The selected boxes are shown on the spatial map (a). The dashed curve represents summer insolation at 30°N. It is worth mentioning here that the EAS region in the tagging experiments covers the Chinese continent up to 45°N and 100°E.*

Deleted: *2*

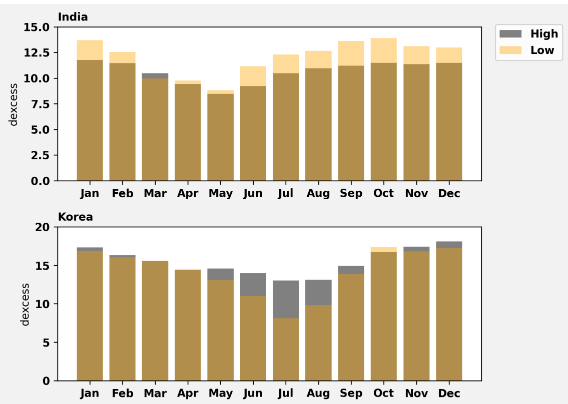

Fig. S14, *d-excess monthly climatology for low precession (Low) and high precession (High) over the Indian and the Korean regions.*

Deleted: *3*

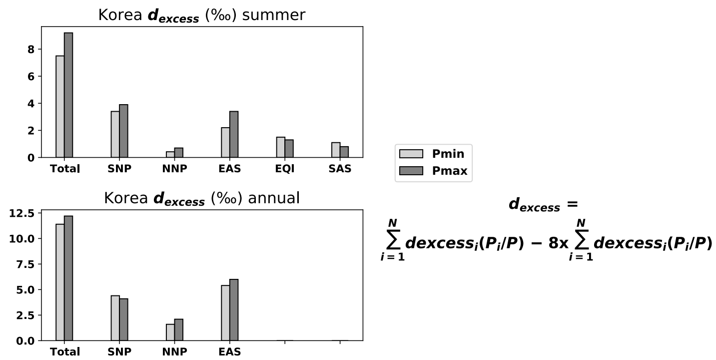

Figure S15; *The summer and annual precipitation d-excess in Korea from major and near-source contributors from land and ocean. "Total" represents the d-excess from all tag regions to Korea.*

Deleted: *4*

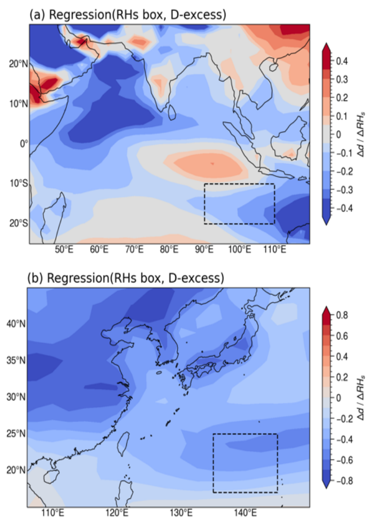

Fig. S16, *(a) Southern Indian Ocean (10-20°S; 90-110°E) and (b) Northwest Pacific Ocean (15-25°N; 135-145°E) surface relative (Rel.) humidity (RHs) regressed over the spatial d-excess(d) values for 130 ka transient simulation. The shading shows slope; Δd/ΔRHs.*

Deleted: *5*

Table S1: *Details on the speleothem stable isotopes records and other proxies used in this study.*

Speleothem-δ^{18}O records			
	~ Ages (ka)	**Location (°N/°E)**	**Reference**
Korea			
1. Eden cave (ED1)	100 – 128, 184 – 209, 397 – 442, 498 – 530	37.10/128.50	(Jo et al., 2011, 2014)
2. Gwaneum cave (GE1)	0.70 – 1.18, 71 – 89	37.32/129.03	
China			
1. Composite	0 – 640	several	(Cheng et al., 2016)
Other proxy records	**~ Ages (ka)**	**Location (°N/°E)**	**Reference**
1. Loess ^{10}Be	0 – 84 and 107 – 550	34.43/107.12	(Beck et al., 2018)
2. U1427 pollen	0.65 – 551	35.96/134.43	(Hayashi et al., 2021)
3. Lake Biwa	1.8 – 134.3 and 0 - 430	~35/~136	(Hayashi et al., 2017; Tarasov et al., 2011)
Atmospheric CO_2			
1. EPICA Dome CO2	0-800	-75.1/158.72	(Lüthi et al., n.d.)

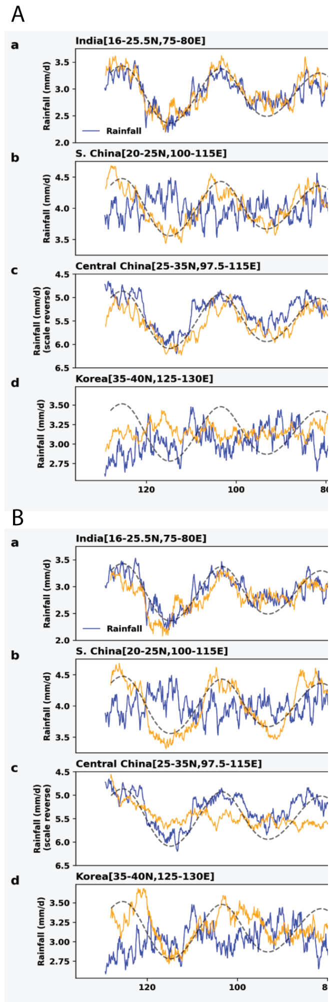

Moved up [1]:

Fig. S16. *Simulated annual mean variations in precipitation (blue curves) for (a) India, (b) South (S.) China, (c) central China, and (d) Korea in the last 130ka from an orbitally forced transient simulation conducted with iCESM1.2. Orange curves in panel A (B) show precipitation-δ^{18}O (d-excess). Dashed black curves represent insolation (30 °N) insolation changes.*

Deleted: Page Break

Table S2: *Tagging results. Blank spaces indicate tag regions not used in the total calculation (column "Total"), as they have no contribution to the anomalous $\delta^{18}O_p$ (Pmin- Pmax).*

(a) d18O																	
	SNP			NNP			EAS			EQI			SAS			Total	
Annual	Pi	d18Oi	d18Oi*(Pi/P)	Pi	d18Oi	d18Oi*(Pi/P)	Pi	d18Oi	d18Oi*(Pi/P)	Pi	d18Oi	d18Oi*(Pi/P)	Pi	d18Oi	d18Oi*(Pi/P)	P	d18O
Pmax	0.99	-11.26	-3.43	0.44	-4.49	-0.62	1.31	-5.32	-2.16	0.2773	-16.81	-1.44	0.215	-16.67	-1.11	3.24	-8.76
Pmin	1.01	-12.31	-4.34	0.34	-4.07	-0.48	1.16	-4.13	-1.68	0.1955	-19.36	-1.32	0.159	-19.09	-1.06	2.86	-8.88
Pmin - Pmax	0.023		-0.91			0.14			0.48			0.12			0.05	-0.37	-0.12
Pmax	0.99	-11.26	-4.05	0.44	-4.49	-0.73	1.31	-5.32	-2.55							2.74	-7.32
Pmin	1.01	-12.31	-4.96	0.34	-4.07	-0.55	1.16	-4.13	-1.91							2.51	-7.42
Pmin - Pmax	0.023		-0.91			0.18			0.63							-0.23	-0.09
Summer	Pi	d18Oi	d18Oi*(Pi/P)	Pi	d18Oi	d18Oi*(Pi/P)	Pi	d18Oi	d18Oi*(Pi/P)	Pi	d18Oi	d18Oi*(Pi/P)	Pi	d18Oi	d18Oi*(Pi/P)	P	d18O
Pmax	1.60	-7.48	-2.41	0.37	-4.18	-0.31	1.76	-4.67	-1.66	0.73	-10.26	-1.50	0.502	-9.54	-0.97	4.96	-6.85
Pmin	2.00	-5.76	-2.20	0.23	-5.53	-0.24	1.87	-3.78	-1.35	0.63	-13.35	-1.61	0.518	-12.56	-1.24	5.24	-6.63
Pmin - Pmax	0.400		0.22			0.07			0.31			-0.11			-0.28	0.28	0.22
(b) dD																	
	SNP			NNP			EAS			EQI			SAS			Total	
Annual	Pi	dDi	dDi*(Pi/P)	Pi	dDi	dDi*(Pi/P)	Pi	dDi	dDi*(Pi/P)	Pi	dDi	dDi*(Pi/P)	Pi	dDi	dDi*(Pi/P)	P	d18O
Pmax	0.99	-78.75	-28.33	0.44	-22.89	-3.71	1.31	-30.03	-14.36							2.74	-46.40
Pmin	1.01	-87.61	-35.27	0.34	-20.25	-2.72	1.16	-21.30	-9.86							2.51	-47.85
Pmin - Pmax	0.023		-6.94			0.99			4.49							-0.23	-1.45
	SNP			NNP			EAS			EQI			SAS			Total	
Summer	Pi	dDi	dDi*(Pi/P)	Pi	dDi	dDi*(Pi/P)	Pi	dDi	dDi*(Pi/P)	Pi	dDi	dDi*(Pi/P)	Pi	dDi	dDi*(Pi/P)	P	d18O
Pmax	1.60	-49.11	-15.85	0.37	-25.20	-1.88	1.76	-28.64	-10.17	0.73	-74.25	-10.86	0.502	-68.43	-6.93	4.96	-45.69
Pmin	2.00	-38.14	-14.56	0.23	-35.55	-1.53	1.87	-24.57	-8.74	0.63	-95.66	-11.54	0.518	-89.5	-8.85	5.24	-45.21
Pmin - Pmax	0.400		1.29			0.35			1.42			-0.67			-1.92	0.28	0.48
(c) d-excess																	
	SNP			NNP			EAS			EQI			SAS			Total	
Annual	Pi	dex_i	dex_i*(Pi/P)	Pi	dex_i	dex_i*(Pi/P)	Pi	dex_i	dex_i*(Pi/P)	Pi	dex_i	dex_i*(Pi/P)	Pi	dex_i	dex_i*(Pi/P)	P	dexc
Pmax	0.99	11.33	4.08	0.44	13.00	2.11	1.31	12.55	6.00							2.74	12.19
Pmin	1.01	10.87	4.38	0.34	12.29	1.65	1.16	11.76	5.45							2.51	11.47
Pmin - Pmax	0.023		0.30			-0.46			-0.55							-0.23	-0.71
	SNP			NNP			EAS			EQI			SAS			Total	
Summer	Pi	dex_i	dex_i*(Pi/P)	Pi	dex_i	dex_i*(Pi/P)	Pi	dex_i	dex_i*(Pi/P)	Pi	dex_i	dex_i*(Pi/P)	Pi	dex_i	dex_i*(Pi/P)	P	dexc
Pmax	1.60	10.73	3.46	0.37	8.20	0.61	1.76	8.70	3.09	0.73	7.83	1.15	0.502	7.89	0.80	4.96	9.11
Pmin	2.00	7.94	3.03	0.23	8.71	0.37	1.87	5.67	2.02	0.63	11.14	1.34	0.518	10.98	1.09	5.24	7.85
Pmin - Pmax	0.400		-0.43			-0.24			-1.07			0.20			0.29	0.28	-1.26

***Table S3**: Korean Speleothem-$\delta^{18}O$ records.*

(a) Eden Cave		(b) Gwaneum Cave	
Age (ka BP)	**$\delta^{18}O$ (‰, VPDB)**	**Age (ka BP)**	**δ18O (‰, VPDB)**
128.19	-7.14	89.00	-8.95
127.77	-7.04	88.83	-8.98
127.34	-7.21	88.66	-8.81
126.49	-7.18	88.49	-9.04
126.06	-7.09	88.32	-9.00
125.63	-7.37	88.15	-8.78
125.21	-7.22	87.98	-8.66
124.78	-7.58	87.81	-8.70
124.36	-7.54	87.64	-8.48
123.93	-7.65	87.47	-8.57
123.50	-7.39	87.30	-8.70
123.08	-7.45	87.13	-8.56
122.22	-7.13	86.96	-8.76
121.80	-6.91	86.79	-8.67
121.37	-7.13	86.62	-8.63
120.94	-6.93	86.45	-8.60
120.52	-7.15	86.28	-8.58
120.09	-6.93	86.11	-8.82
119.66	-7.13	85.94	-8.84
119.24	-7.12	85.77	-8.77
118.81	-7.47	85.60	-8.74
118.39	-7.48	85.43	-8.52
117.96	-7.65	85.26	-8.78
117.53	-7.80	85.09	-8.61
117.11	-8.11	84.92	-8.37
116.68	-7.20	84.75	-8.32
116.25	-8.13	84.58	-8.25
115.83	-8.12	84.41	-8.43
115.40	-8.10	84.24	-8.79
114.97	-7.94	84.07	-8.58
114.55	-8.08	83.90	-8.59
114.12	-7.84	83.73	-8.60
113.70	-8.12	83.56	-8.34
113.27	-8.07	83.39	-8.13
112.84	-8.08	83.22	-8.27
112.42	-8.04	83.05	-8.39
111.99	-8.32	82.88	-8.18
111.56	-8.16	82.71	-8.40
111.14	-8.02	82.54	-8.64

110.71	-8.04	82.37	-8.52
110.28	-8.04	82.20	-8.49
108.70	-7.78	82.03	-8.37
107.12	-8.07	81.86	-8.32
105.54	-7.59	81.69	-8.38
103.96	-8.10	81.52	-8.17
102.38	-7.66	81.35	-8.21
100.80	-8.31	81.18	-8.24
		81.01	-8.25
209.89	-7.90	80.84	-8.14
206.62	-7.85	80.67	-8.27
204.98	-7.83	80.50	-8.27
203.35	-7.89	80.33	-8.53
201.71	-7.60	80.16	-8.03
200.08	-7.82	79.99	-8.36
199.54	-8.38	79.82	-8.47
199.01	-8.08	79.65	-8.20
198.47	-7.94	79.48	-8.29
197.93	-7.95	79.31	-8.40
197.40	-7.04	79.14	-8.30
196.86	-8.26	78.97	-8.57
196.33	-8.13	78.80	-8.56
195.79	-7.87	78.63	-8.63
195.26	-7.94	78.46	-8.54
194.72	-8.17	78.29	-8.46
194.18	-7.97	78.12	-8.35
193.65	-7.58	77.95	-8.75
193.11	-8.06	77.78	-8.41
192.58	-8.42	77.61	-8.43
192.04	-7.80	77.44	-8.34
191.51	-8.23	77.27	-8.36
190.97	-8.32	77.10	-8.37
190.43	-8.37	76.93	-8.30
189.90	-8.23	76.76	-8.39
189.36	-8.33	76.59	-8.25
189.10	-8.09	76.42	-8.38
188.83	-8.05	76.25	-8.25
188.57	-7.66	76.08	-8.15
188.31	-7.75	75.91	-8.03
188.04	-7.55	75.74	-7.94
187.78	-7.47	75.57	-7.92
187.51	-7.42	75.40	-8.19
187.25	-7.26	75.23	-7.86

186.98	-6.90	75.06	-8.29
186.72	-7.09	74.89	-8.22
186.45	-6.98	74.72	-8.18
186.19	-6.98	74.55	-8.21
185.93	-6.92	74.38	-8.31
185.66	-7.11	74.21	-8.23
185.40	-7.72	74.04	-8.15
185.13	-7.97	73.87	-8.33
184.87	-8.03	73.70	-8.10
184.60	-7.81	73.53	-8.02
		73.36	-8.11
441.84	-7.77	73.19	-8.05
441.72	-7.90	73.02	-7.77
441.60	-7.63	72.85	-7.94
441.48	-7.64	72.68	-8.19
441.36	-7.62	72.51	-8.01
441.24	-7.61	72.34	-7.74
441.13	-7.66	72.17	-8.20
441.01	-7.79	72.00	-8.25
440.89	-7.35	71.83	-8.23
440.77	-7.44	71.66	-8.24
440.65	-6.92	71.49	-8.30
440.53	-6.97		
440.42	-6.67	1.18	-8.45
440.30	-6.70	1.12	-8.50
440.18	-6.63	1.06	-8.70
440.06	-6.37	1.00	-8.16
439.94	-6.04	0.94	-8.32
439.82	-6.32	0.88	-7.77
439.71	-6.21	0.82	-8.24
439.59	-6.44	0.76	-7.68
439.47	-6.03	0.70	-7.78
439.35	-7.01		
439.23	-7.61		
439.11	-8.63		
439.00	-8.60		
438.88	-8.15		
438.64	-8.30		
438.52	-8.83		
438.40	-8.78		
438.17	-8.99		
438.05	-8.50		
437.93	-8.94		

437.81	-8.56
437.69	-8.67
437.58	-7.73
437.46	-8.21
437.22	-8.03
436.99	-8.58
436.76	-8.51
436.52	-8.54
436.29	-8.22
436.06	-8.40
435.82	-8.69
435.59	-9.14
435.36	-9.08
435.12	-8.66
434.89	-8.20
434.66	-8.43
434.42	-8.30
434.19	-8.79
433.96	-8.72
433.72	-8.83
433.49	-8.52
433.26	-8.96
433.02	-8.63
432.79	-8.85
432.56	-8.69
432.32	-9.01
432.09	-8.68
431.86	-8.95
431.62	-8.51
431.39	-8.62
431.16	-8.55
430.92	-8.61
430.69	-8.69
430.46	-8.87
430.22	-8.65
429.99	-8.81
429.76	-8.89
429.52	-8.55
429.29	-8.26
429.06	-8.67
428.82	-8.50
428.59	-8.92
428.36	-8.74

428.12	-8.84
427.89	-8.60
427.66	-8.47
427.42	-8.42
427.19	-8.63
426.96	-8.71
426.72	-8.77
426.49	-8.68
426.26	-8.49
425.35	-8.61
424.44	-8.67
423.53	-8.28
422.63	-8.34
421.72	-8.29
420.81	-8.34
419.90	-8.31
418.99	-8.69
418.09	-8.36
417.18	-8.27
416.27	-7.95
415.36	-8.12
414.45	-8.28
413.55	-8.96
412.64	-8.70
411.73	-8.27
410.82	-8.31
409.91	-8.29
409.00	-7.36
408.10	-8.13
407.19	-8.01
406.28	-7.94
405.37	-7.95
404.46	-8.28
403.56	-7.96
402.65	-7.96
401.74	-7.82
400.83	-8.26
399.92	-7.99
399.02	-8.11
398.11	-7.82
397.20	-7.71
529.99	-7.78

528.78	-7.73
527.57	-7.85
526.36	-7.58
525.15	-7.83
523.94	-7.25
522.73	-7.74
521.52	-8.09
520.31	-8.37
519.10	-8.24
517.89	-8.51
516.68	-8.31
515.47	-8.03
514.26	-7.87
513.04	-7.93
511.83	-7.77
510.62	-7.90
509.41	-7.63
508.20	-7.64
506.99	-7.62
505.78	-7.61
504.57	-7.66
503.36	-7.79
502.15	-7.35
500.94	-7.44
499.73	-6.92
498.52	-6.97

SI References

Beck, J. W., Zhou, W., Li, C., Wu, Z., White, L., Xian, F., Kong, X., and An, Z.: A 550,000-year record of East Asian monsoon rainfall from ^{10}Be in loess, Science, 360, 877–881, https://doi.org/10.1126/science.aam5825, 2018.

Cheng, H., Edwards, R. L., Sinha, A., Spötl, C., Yi, L., Chen, S., Kelly, M., Kathayat, G., Wang, X., Li, X., Kong, X., Wang, Y., Ning, Y., and Zhang, H.: The Asian monsoon over the past 640,000 years and ice age terminations, Nature, 534, 640–646, https://doi.org/10.1038/nature18591, 2016.

Hayashi, R., Takahara, H., Inouchi, Y., Takemura, K., and Igarashi, Y.: Vegetation and endemic tree response to orbital-scale climate changes in the Japanese archipelago during the last glacial–interglacial cycle based on pollen records from Lake Biwa, western Japan, Review of Palaeobotany and Palynology, 241, 85–97, https://doi.org/10.1016/j.revpalbo.2017.02.008, 2017.

Hayashi, R., Sagawa, T., Irino, T., and Tada, R.: Orbital-scale vegetation-ocean-atmosphere linkages in western Japan during the last 550 ka based on a pollen record from the IODP site U1427 in the Japan Sea, Quaternary Science Reviews, 267, 107103, https://doi.org/10.1016/j.quascirev.2021.107103, 2021.

Igarashi, Y. and Oba, T.: Fluctuations in the East Asian monsoon over the last 144ka in the northwest Pacific based on a high-resolution pollen analysis of IMAGES core MD01-2421, Quaternary Science Reviews, 25, 1447–1459, https://doi.org/10.1016/j.quascirev.2005.11.011, 2006.

Jo, K., Woo, K. S., Lim, H. S., Cheng, H., Edwards, R. L., Wang, Y., Jiang, X., Kim, R., Lee, J. I., Yoon, H. I., and Yoo, K.-C.: Holocene and Eemian climatic optima in the Korean Peninsula based on textural and carbon isotopic records from the stalagmite of the Daeya Cave, South Korea, Quaternary Science Reviews, 30, 1218–1231, https://doi.org/10.1016/j.quascirev.2011.02.012, 2011.

Jo, K., Woo, K. S., Yi, S., Yang, D. Y., Lim, H. S., Wang, Y., Cheng, H., and Edwards, R. L.: Mid-latitude interhemispheric hydrologic seesaw over the past 550,000 years, Nature, 508, 378–382, https://doi.org/10.1038/nature13076, 2014.

Lüthi, D., Le Floch, M., Bereiter, B., Blunier, T., Barnola, J. M., Siegenthaler, U., Raynaud, D., Jouzel, J., Fischer, H., Kawamura, K., and Stocker, T. F.: NOAA/WDS Paleoclimatology - EPICA Dome C - 800KYr CO2 Data, https://doi.org/10.25921/XGZS-GD10, n.d.

Tarasov, P. E., Nakagawa, T., Demske, D., Österle, H., Igarashi, Y., Kitagawa, J., Mokhova, L., Bazarova, V., Okuda, M., Gotanda, K., Miyoshi, N., Fujiki, T., Takemura, K., Yonenobu, H., and Fleck, A.: Progress in the reconstruction of Quaternary climate dynamics in the Northwest Pacific: A new modern analogue reference dataset and its application to the 430-kyr pollen record from Lake Biwa, Earth-Science Reviews, 108, 64–79, https://doi.org/10.1016/j.earscirev.2011.06.002, 2011.

Wen, Q., Liu, Z., Jing, Z., Clemens, S. C., Wang, Y., Yan, M., Ning, L., and Liu, J.: Grand dipole response of Asian summer monsoon to orbital forcing, npj Clim Atmos Sci, 7, 202, https://doi.org/10.1038/s41612-024-00749-4, 2024.